Wetting, adhesion and friction of superhydrophobic and hydrophilic leaves and fabricated micro/nanopatterned surfaces



2008 J. Phys.: Condens. Matter 20 225010

(http://iopscience.iop.org/0953-8984/20/22/225010)

J. Phys.: Condens. Matter **20** (2008) 225010 (24pp) doi:10.1088/0953-8984/20/22/225010

# Wetting, adhesion and friction of superhydrophobic and hydrophilic leaves and fabricated micro/nanopatterned surfaces

**Bharat Bhushan**[1] **and Yong Chae Jung**

Nanotribology Laboratory for Information Storage and MEMS/NEMS (NLIM), The Ohio State University, 201 West 19th Avenue, Columbus, OH 43210-1142, USA

E-mail: Bhushan.2@osu.edu

Received 31 July 2007, in final form 28 September 2007
Published 30 April 2008
Online at stacks.iop.org/JPhysCM/20/225010

**Abstract**

Superhydrophobic surfaces have considerable technological potential for various applications due to their extreme water-repellent properties. When two hydrophilic bodies are brought into contact, any liquid present at the interface forms menisci, which increases adhesion/friction and the magnitude is dependent upon the contact angle. Certain plant leaves are known to be superhydrophobic in nature due to their roughness and the presence of a thin wax film on the leaf surface. Various leaf surfaces on the microscale and nanoscale have been characterized in order to separate out the effects of the microbumps and nanobumps and the wax on the hydrophobicity. The next logical step in realizing superhydrophobic surfaces that can be produced is to design surfaces based on understanding of the leaves. The effect of micropatterning and nanopatterning on the hydrophobicity was investigated for two different polymers with micropatterns and nanopatterns. Scale dependence on adhesion was also studied using atomic force microscope tips of various radii. Studies on silicon surfaces patterned with pillars of varying diameter, height and pitch values and deposited with a hydrophobic coating were performed to demonstrate how the contact angles vary with the pitch. The effect of droplet size on contact angle was studied by droplet evaporation and a transition criterion was developed to predict when air pockets cease to exist. Finally, an environmental scanning electron microscope study on the effect of droplet size of about 20 $\mu$m radius on the contact angle of patterned surfaces is presented. The importance of hierarchical roughness structure on destabilization of air pockets is discussed.

(Some figures in this article are in colour only in the electronic version)

## 1. Introduction

Advances in nanotechnology, including micro/nanoelectromechanical systems (MEMS/NEMS), have stimulated the development of new materials which require hydrophobic surfaces and interfaces with low adhesion and friction (Bhushan 2007). Hydrophobicity of a surface (wettability) is characterized by the static contact angle between a water droplet and the surface. The contact angle depends on several factors including surface energy, roughness, preparation, and cleanliness of the surface. If the liquid wets the surface (referred to as wetting liquid or hydrophilic surface), the value of the contact angle is $0 \leqslant \theta \leqslant 90°$, whereas if the liquid does not wet the surface (referred to as non-wetting liquid or hydrophobic surface), the value of the contact angle is $90° < \theta \leqslant 180°$. A surface is superhydrophobic if it has a water contact angle above 150°. These surfaces are water repellent. For fluid flow applications, in addition to the high contact angle, superhydrophobic surfaces should also have very low

[1] Author to whom any correspondence should be addressed.

 

water contact angle hysteresis. The contact angle hysteresis is the difference between advancing and receding contact angles and it occurs due to roughness and surface heterogeneity. In the case of these surfaces, contact angle hysteresis reflects a fundamental asymmetry of wetting and dewetting and the irreversibility of the wetting/dewetting cycle. It is a measure of energy dissipation during the flow of a droplet along a solid surface. In the case of superhydrophobic surfaces with low water contact angle hysteresis, water droplets roll off the surface (with some slip) and take contaminants with them. They have low drag for fluid flow and low tilt angle. The self-cleaning surfaces are of interest in various applications, including self-cleaning windows, windshields, exterior paints for buildings and navigation ships, utensils, roof tiles, textiles and reduction of drag in fluid flow, e.g., in micro/nanochannels.

When two hydrophilic surfaces come into contact, condensation of water vapor from the environment forms meniscus bridges at asperity contacts which lead to an intrinsic attractive force (Adamson 1990, Israelachvili 1992, Bhushan 1999, 2002, 2003, 2005). This may lead to high adhesion and stiction. Therefore, hydrophobic surfaces are desirable.

Hydrophobic surfaces can be constructed by using low surface energy material coatings such as polytetrafluoroethylene or wax, by increasing surface area by introducing surface roughness and/or the creation of air pockets. Gaseous phase including water vapor, commonly referred to as 'air' in the literature, trapped in the cavities of a rough surface results in a composite solid–air–liquid interface, as opposed to the homogeneous solid–liquid interface (Wenzel 1936, Cassie and Baxter 1944, Nosonovsky and Bhushan 2005, 2006a, 2006b, 2007a, 2007b, 2007c, 2007d, 2008, Jung and Bhushan 2006, 2007, 2008, Bhushan and Jung 2007, Bhushan *et al* 2007). As indicated earlier, for self-cleaning effect and for with low drag for fluid flow applications, surfaces should exhibit high contact angle (between 150° and 180°) as well as low water contact angle hysteresis (Extrand 2002, Kijlstra *et al* 2002, Jung and Bhushan 2006, 2008, Bhushan and Jung 2007). Examples of such surfaces are found in nature, such as *Nelumbo nucifera* (lotus) and *Colocasia esculenta* (Neinhuis and Barthlott 1997, Wagner *et al* 2003), which have high contact angles with water and show strong self-cleaning properties known as the 'lotus effect' (Barthlott and Neinhuis 1997). Lotus is known to be self-cleaning to prevent pathogens from bounding to the leaf surface. Many pathogenic organisms—spores and conidia of most fungi—require water for germination and can infect leaves in the presence of water (Neinhuis and Barthlott 1997). Studies have been carried out to fully characterize the hydrophobic leaf surfaces at the microscale and nanoscale while separating out the effects of the microbumps and the nanobumps, and the hydrophobic compounds, called waxes on the hydrophobicity (Burton and Bhushan 2006, Bhushan and Jung 2006). The wax is present in crystalline tubules, composed of a mixture of aliphatic compounds, principally nonacosanol and nonacosanediols (Koch *et al* 2006). By learning from what is found in nature, one can create roughness on various materials and study their surface properties, leading to successful implementation in applications where water repellency, fluid flow and lower meniscus is important.

Biomimetics involves taking ideas from nature, mimicking them and implementing them in an application. The word biomimetics is derived from a Greek word 'biomimesis' meaning to mimic life. It is known by several names, such as bionics and biognosis. Mimicking lotus effect falls in the field of biomimetics. A number of studies have been carried out to produce artificial biomimetic roughness-induced hydrophobic surfaces (Shibuichi *et al* 1996, Hozumi and Takai 1998, Coulson *et al* 2000, Miwa *et al* 2000, Oner and McCarthy 2000, Feng *et al* 2002, Erbil *et al* 2003, Lau *et al* 2003, Burton and Bhushan 2005, Bhushan and Jung 2007, Jung and Bhushan 2006, 2007, 2008, Bhushan *et al* 2007, Nosonovsky and Bhushan 2007b, 2007c, 2007d, 2008). More recent studies have investigated the stability of the composite interface of artificial superhydrophobic surfaces and the transition from the composite to homogeneous interface. Nosonovsky and Bhushan (2007a, 2007b, 2007d, 2008) suggested that destabilizing factors responsible for such a transition have different characteristic scale lengths, and thus multiscale (hierarchical) roughness plays an important role in stabilizing the composite interface. Based on modeling and experiments, it has been shown that whether the interface is homogeneous or composite may depend on several factors, such as the distribution of the bumps present on the surface and the size of the liquid droplet (Bico *et al* 2002, Marmur 2003, Lafuma and Quéré 2003, Patankar 2003, He *et al* 2003, Li and Amirfazli 2005, Jung and Bhushan 2006, Wier and McCarthy 2006, Bhushan and Jung 2007, Bhushan *et al* 2007, Jung and Bhushan 2007, 2008, Nosonovsky and Bhushan 2005, 2006a, 2006b, 2007a, 2007b, 2007c, 2007d, 2008).

Various criteria have been formulated to predict the energetic transitions from a metastable composite state to a wetted state (Extrand 2004, Patankar 2004, Bhushan *et al* 2007, Jung and Bhushan 2007, 2008, Nosonovsky and Bhushan 2007b, 2007c, 2007d, 2008). Extrand (2004) formulated the transition criterion referred to as the contact line density criterion which was obtained by balancing the drop weight and the surface forces along the contact line. Patankar (2004) proposed a transition criterion based on energy balance. There is an energy barrier in going from higher energy Cassie and Baxter drop to a lower energy Wenzel drop. The most probable mechanism is that the decrease in the gravitational potential energy during the transition helps in overcoming the energy barrier. This energy barrier was estimated by considering an intermediate state in which the water fills the grooves below the contact area of a Cassie and Baxter drop but the liquid–solid contact is yet to be formed at the bottom of the valleys. These criteria were tested on selected experiments from the literature (Bico *et al* 1999, Oner and McCarthy 2000, Yoshimitsu *et al* 2002, He *et al* 2003). Bhushan *et al* (2007) and Nosonovsky and Bhushan (2007b, 2007c) found that the transition occurs at a critical value of the spacing factor, a non-dimensional parameter which is defined as the diameter of the pillars divided by the pitch distance between them for patterned surfaces, and its ratio to the droplet size. Bhushan and Jung (2007) and Jung and Bhushan (2007, 2008) proposed the transition criterion based on the pitch distance between the pillars and the curvature of droplet governed by the

Laplace equation, which relates pressure inside the droplet to its curvature. In addition, the transition can occur by applying external pressure on the droplet, or by the impact of droplet on the patterned surfaces (Lafuma and Quéré 2003, Callies and Quere 2005, Bartolo *et al* 2006, Reyssat *et al* 2006).

Evaporation studies are useful in characterizing wetting behavior because droplet with various sizes can be created to evaluate the transition criterion on a patterned surface. Many researchers have considered the evaporation of small droplets of liquid on solid surfaces (Bourges-Monnier and Shanahan 1995, Rowan *et al* 1995, Erbil *et al* 2002, Jung and Bhushan 2007, 2008, Nosonovsky and Bhushan 2007c, 2007d, 2008). They developed models to calculate the diffusion of the water droplets into the surrounding atmosphere and compared the experimental data with the models. It has been shown that the wetting state changes from Cassie and Baxter state to Wenzel state as the droplet becomes smaller than a critical value on patterned surfaces during evaporation (McHale *et al* 2005, Jung and Bhushan 2007, 2008, Nosonovsky and Bhushan 2007c, 2007d, 2008).

An environmental scanning electron microscope (ESEM) can be used to condense or evaporate water droplets on surfaces by adjusting the pressure of the water vapor in the specimen chamber and the temperature of the cooling stage. Transfer of the water droplet has been achieved by a specially designed microinjector device on wool fibers and then imaged at room temperature in ESEM (Danilatos and Brancik 1986). Images of water droplets show strong topographic contrast in ESEM such that reliable contact angle measurements can be made on the surfaces (Stelmashenko *et al* 2001). Water condensation and evaporation studies on synthetic patterned surfaces were carried out by Jung and Bhushan (2008) and Nosonovsky and Bhushan (2007c, 2007d, 2008) where the change of contact angle was related with the surface roughness.

In this article, numerical models which provide relationships between roughness and contact angle are first discussed. The role of microbumps and nanobumps is examined by analyzing surface characterization on the microscape and nanoscale of hydrophobic and hydrophilic leaves. Along with measuring and characterizing surface roughness, the contact angle and adhesion and friction properties of these leaves are also considered. The knowledge gained by examining these properties of the leaves and by quantitatively analyzing the surface structure, will be helpful in designing superhydrophobic surfaces. Micropatterned and nanopatterned polymers (hydrophobic and hydrophilic) are fabricated to validate models and to provide design guidelines for superhydrophobic surfaces. These surfaces are examined by measuring their contact angle. To further examine the effect of meniscus force and real area of contact, scale dependence is considered with the use of AFM tips of various radii. Also in this article, a criterion for the transition from Cassie and Baxter regime to Wenzel regime based on the relationship between the size of water droplet and the length parameter of patterned surfaces is discussed. To investigate how the droplet size influences the transition, a study of droplet evaporation is conducted on silicon surfaces patterned with pillars of two different diameters and heights and with varying pitch values and deposited with a hydrophobic coating. Finally, an environmental scanning electron microscope (ESEM) study on the wetting behavior for a microdroplet with about 20 $\mu$m radius on the patterned Si surfaces is presented.

## 2. Experimental techniques

### *2.1. Contact angle, surface roughness, adhesion and friction*

The static- and dynamic (advancing and receding) contact angles, a measure of surface hydrophobicity, were measured using a Rame–Hart model 100 contact angle goniometer and water droplets of deionized water (Burton and Bhushan 2006, Bhushan and Jung 2006, Jung and Bhushan 2006). For the measurement of static contact angle, the droplet size should be small but larger than dimension of the structures present on the surfaces. Droplets of about 5 $\mu$l in volume (with diameter of a spherical droplet about 2.1 mm) were gently deposited on the substrate using a microsyringe for the static contact angle. The receding contact angle was measured by the removal of water from a DI water sessile drop ($\sim$5 $\mu$l) using a microsyringe. The advancing contact angle was measured by adding additional water to the sessile drop ($\sim$5 $\mu$l) using the microsyringe. The contact angle hysteresis was calculated by the difference between the measured advancing and receding contact angles. The tilt angle was measured by a simple stage tilting experiment with the droplets of 5 $\mu$l volume (Bhushan and Jung 2007). All measurements were made by five different points for each sample at 22 $\pm$ 1 °C and 50 $\pm$ 5% RH. The measurements were reproducible to within $\pm$3°.

For surface roughness, an optical profiler (NT-3300, Wyko Corp., Tuscon, AZ) was used for different surface structures (Burton and Bhushan 2006, Bhushan and Jung 2006, 2007, Bhushan *et al* 2007, Jung and Bhushan 2008). A greater $Z$-range of the optical profiler of 2 mm is a distinct advantage over the surface roughness measurements using an AFM which has a $Z$-range of 7 $\mu$m, but it has a maximum lateral resolution of approximately 0.6 $\mu$m (Bhushan 1999, 2002). For additional surface roughness measurements with high lateral resolution and adhesion and friction measurements, a commercial AFM (D3100, Nanoscope IIIa controller, Digital Instruments, Santa Barbara, CA) was used (Burton and Bhushan 2005, Bhushan and Jung 2006, Jung and Bhushan 2006). In order to measure surface roughness, experiments were performed using a square pyramidal Si(100) tip with a native oxide layer which has a nominal radius of 20 nm on a rectangular Si(100) cantilever with a spring constant of 3 N m$^{-1}$ in tapping mode. Experiments were performed using three different radii tips to study the effect of scale dependence. Large radii atomic force microscopy (AFM) tips were primarily used in this study. Borosilicate ball with 15 $\mu$m radius and silica ball with 3.8 $\mu$m radius were mounted on a gold-coated triangular $Si_3N_4$ cantilever with a nominal spring constant of 0.58 N m$^{-1}$. A square pyramidal $Si_3N_4$ tip with nominal radius 30–50 nm on a triangular $Si_3N_4$ cantilever with a nominal spring constant of 0.58 N m$^{-1}$ was used for smaller radius tip. Adhesion and friction at varying relative humidity were measured using a 15 $\mu$m radius borosilicate ball. A large tip radius was used to

measure contributions from micropatterned and nanopatterned surfaces. Friction force was measured under a constant load using a 90° scan angle at a velocity of 100 $\mu$m s$^{-1}$ in 50 $\mu$m and at a velocity of 4 $\mu$m s$^{-1}$ in 2 $\mu$m scans. Adhesive force was measured using the single-point measurement of a force calibration plot (Bhushan 1999, 2002, 2003, 2005).

### 2.2. Measurement of droplet evaporation

The process of the droplet evaporation was obtained by a digital camcorder (Sony, DCRSR100) with a 10× optical and 120× digital zoom for each experimental run and then measuring the decrease in the diameter of droplet as a function of time (Jung and Bhushan 2007, 2008). Frame by frame advancement of the camcorder gave a resolution of 0.03 s. An objective lens placed in front of the camcorder during recording gave a total magnification of between 10 and 20 times. Droplet diameters as small as few hundred microns can be recorded. Droplets were gently deposited on the substrate using a microsyringe and the whole process of evaporation was recorded. The evaporation starts right after the deposition of the droplets. Images obtained were analyzed using Imagetool® software (University of Texas Health Science Center) for the contact angle. To find dust trace remaining after droplet evaporation, an optical microscope with a CCD camera (Nikon, Optihot-2) was used. All measurements were made in a controlled environment at 22 ± 1 °C and 45 ± 5% RH.

### 2.3. Measurement of contact angle using ESEM

A Philips XL30 ESEM equipped with a Peltier cooling stage was used to study smaller droplets (Jung and Bhushan 2008). ESEM uses a gaseous secondary electron detector (GSED) for imaging. The ESEM column is equipped with a multistage differential pressure pumping unit. The pressure in the upper part is about $10^{-6}$–$10^{-7}$ Torr, but a pressure of about 1–15 Torr can be maintained in the observation chamber. When the electron beam (primary electrons) ejects secondary electrons from the surface of the sample, the secondary electrons collide with gas molecules in the ESEM chamber, which in turn function as a cascade amplifier, delivering the secondary electron signal to the positively biased GSED. The positively charged ions are attracted toward the specimen to neutralize the negative charge produced by the electron beam. Therefore, the ESEM can be used to examine electrically insulative specimens in their natural state. In ESEM, adjusting the pressure of the water vapor in the specimen chamber and the temperature of the cooling stage will allow the water to condense on the sample in the chamber. For the measurement of static contact angle and hysteresis angle on patterned surfaces, the video images were recorded. The voltage of the electron beam was 15 kV and the distance of the specimen from the final aperture was about 8 mm. If the angle of observation is not parallel to the surface, the electron beam is not parallel to the surface but inclined at an angle, this will produce a distortion in the projection of the droplet profile. A mathematical model to calculate the real contact angle from the ESEM images was used to correct the tilting of the surfaces during imaging (Brugnara *et al* 2006, Jung and Bhushan 2008).

## 3. Contact angle analysis for a liquid droplet in contact with a rough surface

As stated in section 1, superhydrophobic surfaces should have both high contact angle and low contact angle hysteresis. Liquid may form either homogeneous interface with a solid, or a composite interface with air pockets trapped between the solid and liquid. In this section, mathematical models which provide relationships between roughness and contact angle are discussed.

### 3.1. Homogeneous interface

Consider a rough solid surface with a typical size of roughness details smaller than the size of the droplet as shown in figure 1(a). For a droplet in contact with a rough surface without air pockets, referred to as homogeneous interface, the contact angle is given as (Wenzel 1936)

$$\cos\theta = R_f \cos\theta_0, \tag{1}$$

where $\theta$ is the contact angle for rough surface, $\theta_0$ is the contact angle for smooth surface, and $R_f$ is a roughness factor defined as a ratio of the solid–liquid area $A_{SL}$ to its projection on a flat plane, $A_F$

$$R_f = \frac{A_{SL}}{A_F}. \tag{2}$$

The dependence of the contact angle on the roughness factor is presented in figure 1(b) for different values of $\theta_0$, based on equation (1). The model predicts that a hydrophobic surface ($\theta_0 > 90°$) becomes more hydrophobic with an increase in $R_f$ and a hydrophilic surface ($\theta_0 < 90°$) becomes more hydrophilic with an increase in $R_f$ (Nosonovsky and Bhushan 2005, Jung and Bhushan 2006). A simplest structure to increase $R_f$ would be hemispherically topped cylindrical asperities. To have one hundred per cent packing density, one could use pyramidal asperities with rounded tops (figure 1(c)) (Nosonovsky and Bhushan 2005).

### 3.2. Composite interface

For a rough surface, a wetting liquid will be completely absorbed by the rough surface cavities while a non-wetting liquid may not penetrate into surface cavities, resulting in the formation of air pockets, leading to a composite solid–liquid–air interface as shown in figure 2(a). Cassie and Baxter (1944) extended Wenzel equation for the composite interface, which was originally developed for the homogeneous solid–liquid interface. For this case, there are two sets of interfaces: a solid–liquid interface with the ambient environment surrounding the droplet and a composite interface involving liquid–air and solid–air interfaces. In order to calculate the contact angle for the composite interface, Wenzel equation can be modified by combining the contribution of the fractional area of wet surfaces and the fractional area with air pockets ($\theta = 180°$)

$$\cos\theta = R_f \cos\theta_0 - f_{LA}(R_f \cos\theta_0 + 1) \tag{3}$$

where $f_{LA}$ is fractional flat geometrical areas of the liquid–air interfaces under the droplet. The dependence of the contact

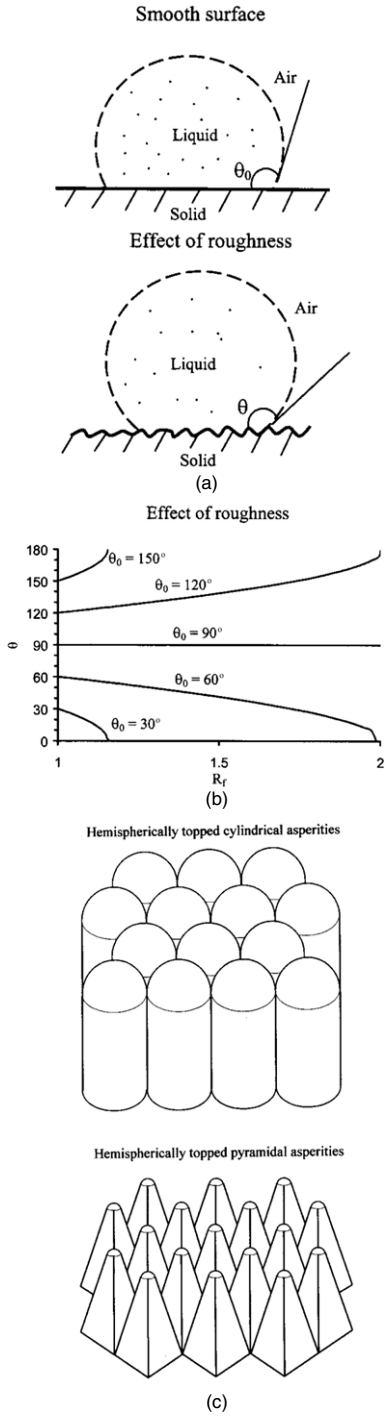


**Figure 1.** (a) Droplet of liquid in contact with a solid surface—smooth surface, contact angle $\theta_0$; rough surface, contact angle $\theta$, (b) contact angle for rough surface ($\theta$) as a function of the roughness factor ($R_f$) for various contact angles of the smooth surface ($\theta_0$), and (c) examples of roughness distribution—hemispherically topped cylindrical asperities and pyramidal asperities with square foundation and rounded tops (Nosonovsky and Bhushan 2005).

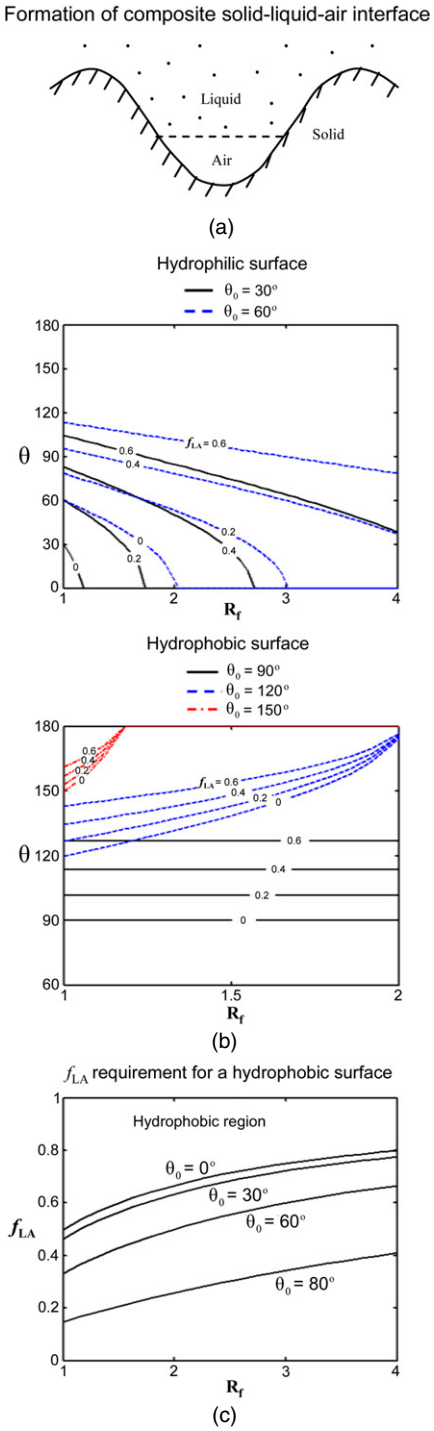


**Figure 2.** (a) Formation of a composite solid–liquid–air interface for rough surface, (b) contact angle for rough surface ($\theta$) as a function of the roughness factor ($R_f$) for various $f_{LA}$ values on the hydrophilic surface and the hydrophobic surface, and (c) $f_{LA}$ requirement for a hydrophilic surface to be hydrophobic as a function of the roughness factor ($R_f$) and $\theta_0$ (Jung and Bhushan 2006).

angle on the roughness factor for hydrophilic and hydrophobic surfaces is presented in figure 2(b). This model shows that for a hydrophilic surface, contact angle on a smooth surface increases with an increase of $f_{LA}$. When roughness factor increases, the contact angle decreases but at a slower rate, due to formation of the composite interface. At a high value of $f_{LA}$, surface can become hydrophobic; however, the value required may be unachievable or formation of air pockets may become unstable. For the hydrophobic surface, contact angle increases with an increase in $f_{LA}$ both for smooth and rough surfaces.

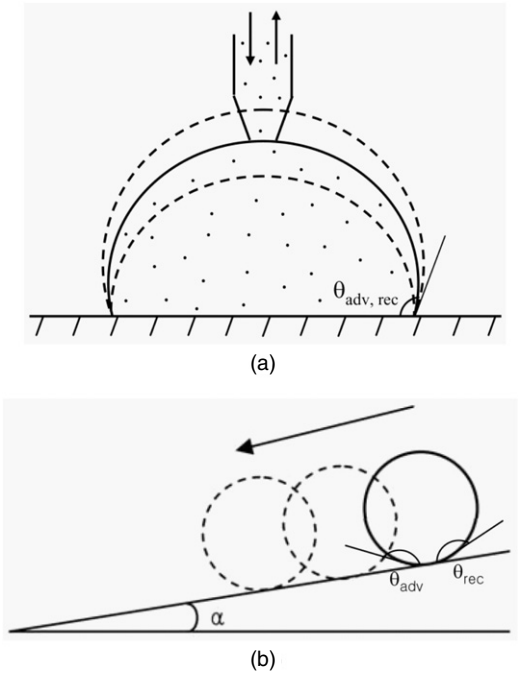


**Figure 3.** (a) Liquid droplet in contact with rough surface (advancing and receding contact angles are $\theta_{adv}$ and $\theta_{rec}$, respectively) and (b) tilted surface profile (the tilt angle is $\alpha$) with a liquid droplet.

Using equation (3), $f_{LA}$ requirement for a hydrophilic surface to be hydrophobic can be found as (Jung and Bhushan 2006)

$$f_{LA} \geqslant \frac{R_f \cos\theta_0}{R_f \cos\theta_0 + 1} \qquad \text{for } \theta_0 < 90^\circ. \tag{4}$$

Figure 2(c) shows the value of $f_{LA}$ requirement as a function of $R_f$ for four surfaces with different contact angles, $\theta_0$. Hydrophobic surfaces can be achieved above a certain $f_{LA}$ values as predicted by equation (4). The upper part of each contact angle line is hydrophobic region. When $R_f$ increases, $f_{LA}$ requirement also increases.

Another important characteristic of a solid–liquid interface is the contact angle hysteresis ($\theta_H$) which is the difference between the contact angle at the increased droplet volume (advancing contact angle, $\theta_{adv}$) and the contact angle at the decreased droplet volume (receding contact angle, $\theta_{rec}$) for a droplet on the solid surface (figure 3(a)). The contact angle hysteresis occurs due to surface roughness and heterogeneity. Low contact angle hysteresis results in a very low water roll-off angle, which denotes the angle to which a surface may be tilted for roll-off of water drops (i.e., very low water contact angle hysteresis) (Extrand 2002, Kijlstra *et al* 2002, Bhushan and Jung 2007, Jung and Bhushan 2008) (figure 3(b)). Low water roll-off angle is important in liquid flow applications such as in micro/nanochannels and surfaces with self-cleaning ability. It is understood that during roll-off of water droplets, some slip is associated.

There is no simple expression for the contact angle hysteresis as a function of roughness; however, certain conclusions about the relation of the contact angle hysteresis to roughness can be made. Using equation (3), the difference of cosines of the advancing and receding angles is related to the difference of those for a nominally smooth surface, $\theta_{adv0}$ and $\theta_{rec0}$, as (Bhushan *et al* 2007, Nosonovsky and Bhushan 2007a)

$$\cos\theta_{adv} - \cos\theta_{rec} = R_f(1 - f_{LA})(\cos\theta_{adv0} - \cos\theta_{rec0}) + H_r, \tag{5}$$

where $H_r$ is the effect of surface roughness, which is equal to the total perimeter of the asperity per unit area. It is observed from equations (3) and (5), that increasing $f_{LA} \to 1$ results in increasing the contact angle ($\cos\theta \to -1, \theta \to \pi$) and decreasing the contact angle hysteresis ($\cos\theta_{adv} - \cos\theta_{rec} \to 0$). In the limiting case of very small solid–liquid fractional contact area under the droplet, when the contact angle is large ($\cos\theta \approx -1 + (\theta - \pi)^2/2$, $\sin\theta \approx \pi - \theta$) and the contact angle hysteresis is small ($\theta_{adv} \approx \theta \approx \theta_{rec}$), equations (3) and (5) are reduced to

$$\theta - \pi = \sqrt{2(1 - f_{LA})(R_f \cos\theta_0 + 1)} \tag{6}$$

$$\theta_{adv} - \theta_{rec} = (1 - f_{LA}) R_f \frac{\cos\theta_{a0} - \cos_{r0}}{\sin\theta}$$

$$= (\sqrt{1 - f_{LA}}) R_f \frac{\cos_{r0} - \cos_{a0}}{\sqrt{2(R_f \cos\theta_0 + 1)}}. \tag{7}$$

For the homogeneous interface, $f_{LA} = 0$, whereas for composite interface $f_{LA}$ is not a zero number. It is observed from equations (5)–(7) that for homogeneous interface, increasing roughness (high $R_f$) leads to increasing the contact angle hysteresis (high values of $\theta_{adv} - \theta_{rec}$), while for composite interface, an approach to unity of $f_{LA}$ provides with both high contact angle and small contact angle hysteresis (Jung and Bhushan 2006, Bhushan *et al* 2007, Nosonovsky and Bhushan 2007a, 2007b). Therefore, the composite interface is desirable for superhydrophobicity.

Formation of a composite interface is also a multiscale phenomenon, which depends upon relative sizes of the liquid droplet and roughness details. The composite interface is fragile and can be irreversibly transformed into the homogeneous interface, thus damaging superhydrophobicity. In order to form a stable composite interface with air pockets between solid and liquid, the destabilizing factors such as capillary waves, nanodroplet condensation, and liquid pressure should be avoided. For high $f_{LA}$, nanopattern is desirable because whether liquid–air interface is generated depends upon the ratio of distance between two adjacent asperities and droplet radius. Furthermore, nanoscale asperities can pin liquid droplets and thus prevent liquid from filling the valleys between asperities. High $R_f$ can be achieved by both micropatterns and nanopatterns. Nosonovsky and Bhushan (2007a, 2007b, 2007d) have demonstrated that a combination of microroughness and nanoroughness (multiscale roughness) can help to resist the destabilization, with convex surfaces pinning the interface and thus leading to stable equilibrium as well as preventing from filling the gaps between the pillars even in the case of a hydrophilic material. The effect of roughness on wetting is scale dependent and mechanisms that lead to destabilization of a composite interface are also scale dependent. To effectively resist these scale-dependent mechanisms, it is expected that a multiscale roughness is optimum for superhydrophobicity (Nosonovsky and Bhushan 2007a, 2007b, 2007d).

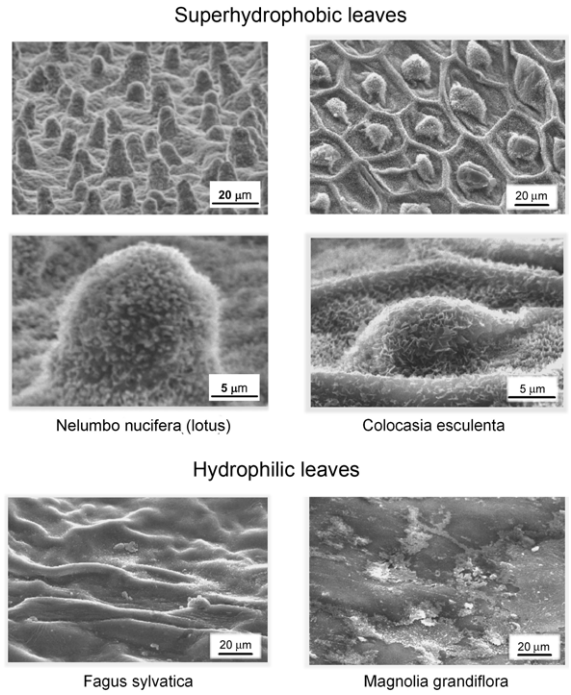


**Figure 4.** Scanning electron micrographs of the relatively rough, water-repellent leaf surfaces of *Nelumbo nucifera (lotus) and Colocasia esculenta* and the relatively smooth, wettable leaf surfaces of *Fagus sylvatica and Magnolia grandiflora* (Bhushan and Jung 2006).

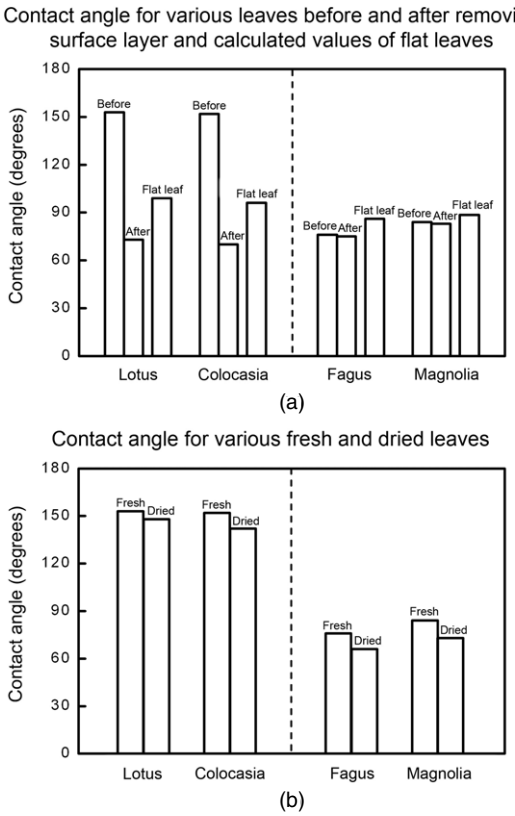


**Figure 5.** Contact angle measurements and calculations for the leaf surfaces: (a) before and after removing surface layer as well as calculated values, and (b) fresh and dried leaves. The contact angle on a smooth surface for the four leaves was obtained using the roughness factor calculated (Bhushan and Jung 2006).

## 4. Characterization of hydrophobic and hydrophilic leaf surfaces

In order to completely understand the nature of hydrophobic and hydrophilic leaves, a comprehensive characterization of the surface and its properties must be carried out. Using the various characterization techniques discussed previously, the surfaces of the leaves have been measured so that an understanding of the factors that are responsible for its hydrophobic/hydrophilic nature can be accomplished (Bhushan and Jung 2006, Burton and Bhushan 2006). Below is a discussion of the findings of the study.

### *4.1. Hydrophobic and hydrophilic leaves*

Figure 4 shows the micrographs of two hydrophobic leaves—lotus (*Nelumbo nucifera*) and colocasia (*Colocasia esculenta*)—and two hydrophilic leaves—fagus (*Fagus sylvatica*) and magnolia (*Magnolia grandiflora*)—measured using scanning electron microscopy (SEM) (Bhushan and Jung 2006). Lotus and colocasia are characterized by papillose epidermal cells responsible for creation of papillae or bumps on the surfaces, and an additional layer of epicuticular waxes which are mixture of large hydrocarbon molecules. Fagus and magnolia are characterized by sunken and raised nerves, respectively (Barthlott and Neinhuis 1997).

### *4.2. Contact angle measurements*

Figure 5(a) shows the contact angles for the hydrophobic and hydrophilic leaves before and after using acetone. After using acetone in order to remove any wax present on the surface, for the hydrophobic leaves the contact angle dramatically reduced but on the contrary, for the hydrophilic leaves the contact angle was almost unchanged. This suggests that wax does not exist on the hydrophilic leaves. In contrast, hydrophobic leaves have a thin wax film on the surface of the leaf and consequently, the combination of this wax and the roughness of the leaf creates a superhydrophobic surface.

Bhushan and Jung (2006) calculated the contact angles for leaves with smooth surface using equation (1) and the calculated $R_f$ (to be presented later) and the contact angle of the four leaves. These are also presented in figure 5(a). The approximate values of $R_f$ for lotus and colocasia are 5.6 and 8.4 and for fagus and magnolia are 3.4 and 3.8, respectively. The contact angles on smooth surface for the four leaves, therefore, can be calculated using these values. Based on the calculations, the contact angles on smooth surface were approximately 99° for lotus and 96° for colocasia. For both fagus and magnolia, the contact angles for the smooth surfaces were found as approximately 86° and 88°. A further discussion on the effect of $R_f$ on the contact angle will be presented later.

Figure 5(b) shows the contact angles for both fresh and dried states for the four leaves. There is a decrease in the contact angle for all four leaves when they are dried. For lotus and colocasia, this decrease is present because it is found that a fresh leaf has taller bumps than a dried leaf

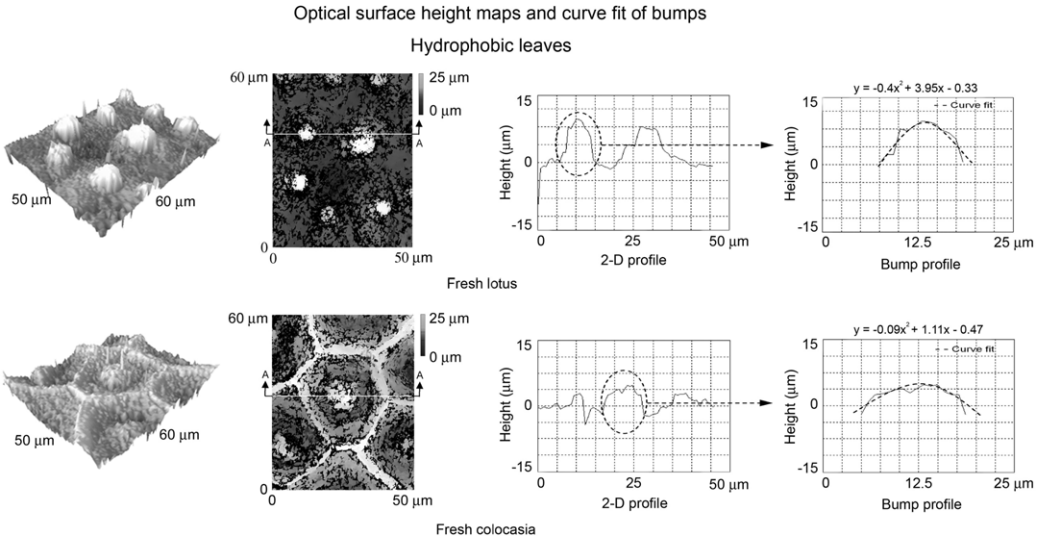


**Figure 6.** Surface height maps and 2D profiles of hydrophobic leaves using an optical profiler. For lotus leaf, a microbump is defined as a single, independent microstructure protruding from the surface. For colocasia leaf, a microbump is defined as the single, independent protrusion from the leaf surface, whereas a ridge is defined as the structure that surrounds each bump and is completely interconnected on the leaf. A curve has been fitted to each profile to show exactly how the bump shape behaves. The radius of curvature is calculated from the parabolic curve fit of the bump (Bhushan and Jung 2006).

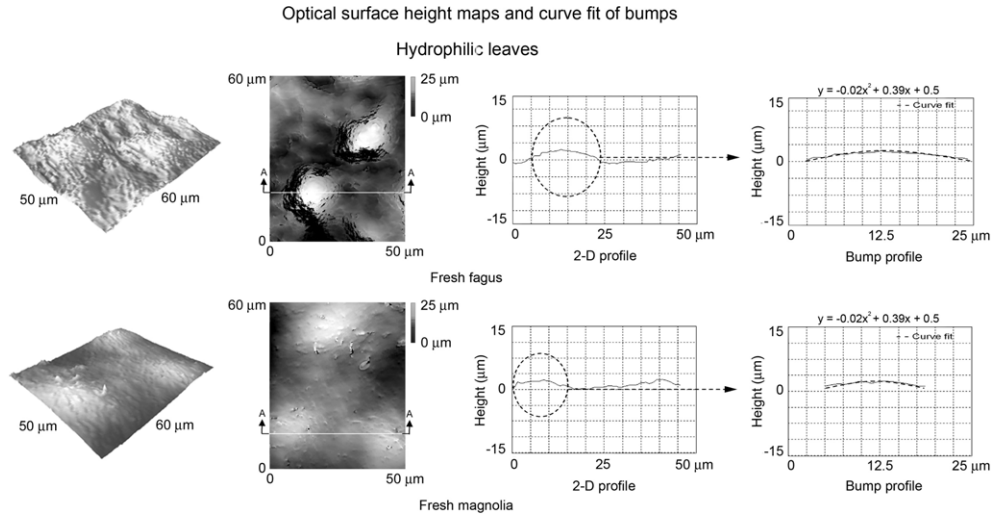


**Figure 7.** Surface height maps and 2D profiles of hydrophilic leaves using an optical profiler. For fagus and magnolia leaves, a microbump is defined as a single, independent microstructure protruding from the surface. A curve has been fitted to each profile to show exactly how the bump shape behaves. The radius of curvature is calculated from the parabolic curve fit of the bump (Bhushan and Jung 2006).

(data to be presented later), which will give a larger contact angle, according to equation (1). When the surface area is at a maximum compared to the footprint area, as with a fresh leaf, the roughness factor will be at a maximum and will only reduce when shrinking has occurred after drying. To understand the reason for the decrease of contact angle after drying of hydrophilic leaves, dried magnolia leaves were also measured using an AFM. It is found that the dried leaf ($P$–$V$ height = 7 $\mu$m, mid-width = 15 $\mu$m, and peak radius = 18 $\mu$m) has taller bumps than a fresh leaf ($P$–$V$height = 3 $\mu$m, mid-width = 12 $\mu$m, and peak radius = 15 $\mu$m), which increases the roughness, and the contact angle decreases, leading to a more hydrophilic surface.

### *4.3. Surface characterization using an optical profiler*

The use of an optical profiler allows measurements to be made on fresh leaves, which have a large $P$–$V$ distance. Three different surface height maps can be seen for hydrophobic and hydrophilic leaves in figures 6 and 7 (Bhushan and Jung 2006). In each figure, a 3D map and a flat map along with a 2D profile in a given location of the flat 3D map are shown. A scan size of 60 $\mu$m × 50 $\mu$m was used to obtain a sufficient amount of bumps to characterize the surface but also to maintain enough resolution to get an accurate measurement.

The structures found with the optical profiler correlate well with the SEM images shown in figure 4. The bumps on the lotus leaf are distributed on the entire surface, but the colocasia

**Table 1.** Microbump and nanobump map statistics for hydrophobic and hydrophilic leaves, measured both fresh and dried leaves using an optical profiler and AFM (Bhushan and Jung 2006).

| | | Microbump ($\mu$m) Scan size ($50\ \mu m \times 50\ \mu m$) | | | Nanobump ($\mu$m) Scan size ($2\ \mu m \times 2\ \mu m$) | | |
|---|---|---|---|---|---|---|---|
| Leaf | | $P$–$V$ height | Mid-width | Peak radius | $P$–$V$ height | Mid-width | Peak radius |
| Lotus | | | | | | | |
| Fresh | | 13[a] | 10[a] | 3[a] | 0.78[b] | 0.40[b] | 0.15[b] |
| Dried | | 9[b] | 10[b] | 4[b] | 0.67[b] | 0.25[b] | 0.10[b] |
| Colocasia | | | | | | | |
| Fresh | Bump | 9[a] | 15[a] | 5[a] | 0.53[b] | 0.25[b] | 0.07[b] |
| | Ridge | 8[a] | 7[a] | 4[a] | 0.68[b] | 0.30[b] | 0.12[b] |
| Dried | Bump | 5[b] | 15[b] | 7[b] | 0.48[b] | 0.20[b] | 0.06[b] |
| | Ridge | 4[b] | 8[b] | 4[b] | 0.57[b] | 0.25[b] | 0.11[b] |
| Fagus | | | | | | | |
| Fresh | | 5[a]<br>4[b] | 10[a]<br>5[b] | 15[a]<br>10[b] | 0.18[b] | 0.04[b] | 0.01[b] |
| Magnolia | | | | | | | |
| Fresh | | 4[a]<br>3[b] | 13[a]<br>12[b] | 17[a]<br>15[b] | 0.07[b] | 0.05[b] | 0.04[b] |

[a] Data measured using optical profiler.
[b] Data measured using AFM.

leaf shows a very different structure to that of the lotus. The surface structure for colocasia not only has bumps similar to lotus but surrounding each bump, a ridge is present that keeps the bumps separated. With these ridges, the bumps have a hexagonal packing geometry which allows for the maximum number of bumps in a given area. The bumps of lotus and both bumps and ridges of colocasia contribute to the hydrophobic nature since they both increase the $R_f$ factor and result in air pockets between the droplet of water and the surface. In fagus and magnolia height maps, short bumps on the surface can be seen. This means that with decreased bump height, the probability of air pocket formation decreases and bumps have a less beneficial effect on the contact angle.

As shown in 2D profiles of hydrophobic and hydrophilic leaves in figures 6 and 7, a curve has been fitted to each profile to show exactly how the bump shape behaves. For each leaf a second order curve fit has been given to the profiles to show how closely the profile is followed. By using the second order curve fit of the profiles, the radius of curvature can be found (Bhushan and Jung 2006, Burton and Bhushan 2006).

Using these optical surface height maps, different statistical parameters of bumps and ridges can be found to characterize the surface: peak to valley ($P$–$V$) height, mid-width, and peak radius (Bhushan 1999, 2002). Here, mid-width is defined as the width of the bump at a height equal to half of peak to mean value. Table 1 shows these quantities found in the optical height maps for four leaves. Comparing the hydrophobic and hydrophilic leaves it can be seen that the $P$–$V$ height for bumps of lotus and colocasia is much taller than that for bumps of fagus and magnolia. The peak radius for bumps of lotus and colocasia is also smaller than that for bumps of fagus and magnolia. However, the values of mid-width for bumps of four leaves are similar.

### *4.4. Leaf characterization using an AFM*

*4.4.1. Comparison of two techniques.* To measure topographic imaging of the leaf surfaces, both contact and tapping modes were first used to characterize the lotus leaf (Bhushan and Jung 2006). Figure 8 shows surface height maps of dried lotus obtained using the two techniques. In contact mode, local height variation for lotus leaf was observed in 50 $\mu$m scan size. However, little height variation was obtained in a 2 $\mu$m scan even at loads as low as 2 nN. This could be due to the substantial frictional force generated as the probe scanned over the sample. The frictional force can damage the sample. The tapping mode technique allows high resolution topographic imaging of sample surfaces that are easily damaged, loosely held to their substrate, or difficult to image by other AFM techniques (Bhushan 1999, 2002). As shown in figure 8, with the tapping mode technique, the soft and fragile leaves can be imaged successfully. Therefore tapping mode technique was used to examine the surface roughness of the hydrophobic and hydrophilic leaves using an AFM.

*4.4.2. Surface characterization.* The AFM has a $Z$-range of about 7 $\mu$m, and cannot be used to make measurements in conventional way because of large $P$–$V$ distance of lotus leaf. Burton and Bhushan (2006) developed a new method to fully determine the bump profiles. In order to compensate for the large $P$–$V$ distance, two scans were made for each height: one measurement that scans the tops of the bumps and another measurement that scans the bottom or valleys of the bumps. The total height of the bumps is embedded within the two scans. Figure 9 shows the 50 $\mu$m surface height maps obtained using this method (Bhushan and Jung 2006). The 2D profiles in the right side column take the profiles from the top scan and

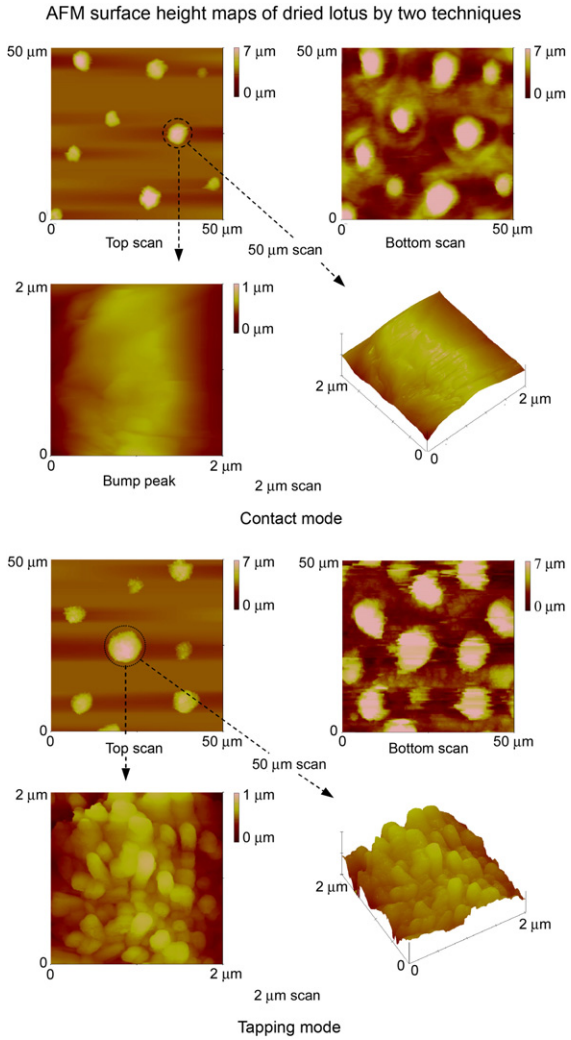


**Figure 8.** Surface height maps showing the top scan and bottom scan in a 50 $\mu$m scan size and the bump peak scan selected in a 2 $\mu$m scan size for a lotus leaf in contact mode and tapping mode. Two methods were tested to get high resolution of nanotopography for a lotus leaf (Bhushan and Jung 2006).

the bottom scan for each scan size and splice them together to get the total profile of the leaf. The 2 $\mu$m surface height maps for both fresh and dried lotus can also be seen in figure 9. This scan area was selected on the top of a microbump obtained in the 50 $\mu$m surface height map. It can be seen that nanobumps are randomly and densely distributed on the entire surface of lotus.

Bhushan and Jung (2006) also measured the surface height maps for the hydrophilic leaves in both 50 $\mu$m and 2 $\mu$m scan sizes as shown in figure 10. For fagus and magnolia, microbumps were found on the surface and the $P$–$V$ distance of these leaves is lower than that of lotus and colocasia. It can be seen in the 2 $\mu$m surface height maps that nanobumps selected on the peak of the microbump have an extremely low $P$–$V$ distance.

Using the AFM surface height maps, different statistical parameters of bumps and ridges can be obtained: $P$–$V$ height, mid-width, and peak radius. These quantities for four leaves are listed in table 1. It can be seen that the values correlate well with the values obtained from optical profiler scans except for the bump heights, which decreases by more than half because of leaf shrinkage.

*4.4.3. Adhesive force and friction.* Adhesive force and coefficient of friction of hydrophobic and hydrophilic leaves using AFM are presented in figure 11 (Bhushan and Jung 2006). For each type of leaf, adhesive force measurements were made for both fresh and dried leaves using a 15 $\mu$m radius tip. It is found that the dried leaves had a lower adhesive force than the fresh leaves. Adhesive force arises from several sources in changing the presence of a thin liquid film such as adsorbed water layer that causes meniscus bridges to build up around the contacting and near-contacting bumps as a result of surface energy effects (Bhushan 1999, 2002). When the leaves are fresh there is moisture within the plant material that causes the leaf to be soft and when the tip comes into contact with the leaf sample, the sample will deform and a larger real area of contact between the tip and sample will occur and the adhesive force will increase. After the leaf has dried, the moisture that was in the plant material is gone, and there is not as much deformation of the leaf when the tip comes into contact with the leaf sample. Hence, the adhesive force is decreased because the real area of contact has decreased.

The adhesive force of fagus and magnolia is higher than that of lotus and colocasia. The reason is that the real area of contact between the tip and leaf sample is expected to be higher in hydrophilic leaves than that in hydrophobic leaves because of their high affinity to water and consequently higher meniscus forces (Bhushan 1999, 2002).

The coefficient of friction was only measured on a dried plant surface with the same sliding velocity (10 $\mu$m s$^{-1}$) in different scan sizes rather than including the fresh surface because the $P$–$V$ was too large to scan back and forth with the AFM to obtain friction force. As expected, the coefficient of friction for hydrophobic leaves is lower than that for hydrophilic leaves due to the real area of contact between the tip and leaf sample, similar to the adhesive force results. When the scan size from microscale to nanoscale decreases, the coefficient of friction also decreases in each leaf. The reason for such dependence is the scale-dependent nature of the roughness of the leaf surface. Figures 9 and 10 show AFM topography images and 2D profiles of the surfaces for different scan sizes. The scan size dependence of the coefficient of friction has been reported previously (Poon and Bhushan 1995, Koinkar and Bhushan 1997, Tambe and Bhushan 2004).

*4.4.4. Role of microbumps versus nanobumps.* The approximation of the roughness factor for the leaves on the micro- and nanoscale was made using AFM scan data (Bhushan and Jung 2006). Roughness factors for various leaves are presented in table 2. As mentioned earlier, the open space between asperities on a surface has the potential to collect air, and its probability appears to be higher in nanobumps as the distance between bumps in the nanoscale is smaller than those in microscale. Using roughness factor values, along with the contact angles ($\theta$) from both hydrophobic and hydrophilic surfaces; 153° and 152° in

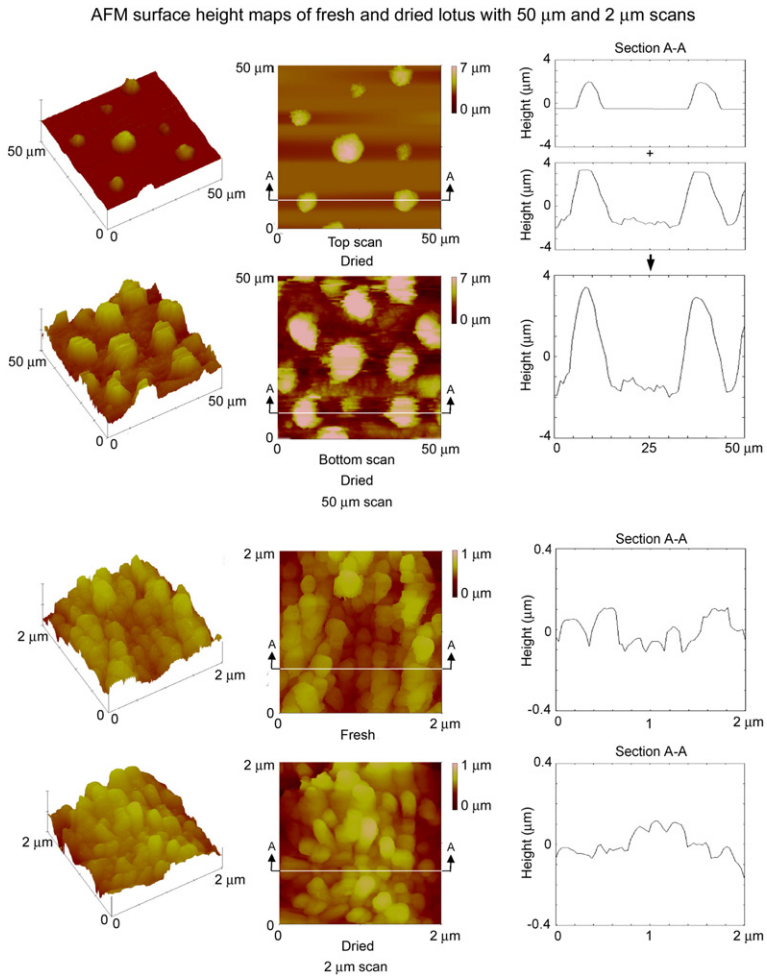


**Figure 9.** Surface height maps and 2D profiles showing the top scan and bottom scan of a dried lotus leaf in 50 $\mu$m scan (because the $P$–$V$ distance of a dried lotus leaf is greater than the $Z$-range of an AFM), and both fresh and dried lotus in a 2 $\mu$m scan (Bhushan and Jung 2006).

**Table 2.** Roughness factor and contact angle ($\Delta\theta = \theta - \theta_0$) calculated using $R_f$ on the smooth surface for hydrophobic and hydrophilic leaves measured using an AFM, both microscale and nanoscale (Bhushan and Jung 2006).

| Leaf (contact angle) | Scan size | State | $R_f$ | $\Delta\theta$ |
|---|---|---|---|---|
| Lotus (153°) | 50 $\mu$m | Dried | 5.6 | 54[a] |
| | 2 $\mu$m | Fresh | 20 | 61[b] |
| | | Dried | 16 | 60[b] |
| Colocasia (152°) | 50 $\mu$m | Dried | 8.4 | 56[a] |
| | 2 $\mu$m bump | Fresh | 18 | 60[b] |
| | | Dried | 14 | 59[b] |
| | 2 $\mu$m ridge | Fresh | 18 | 60[b] |
| | | Dried | 15 | 59[b] |
| Fagus (76°) | 50 $\mu$m | Fresh | 3.4 | −10[a] |
| | 2 $\mu$m | Fresh | 5.3 | 2[b] |
| Magnolia (84°) | 50 $\mu$m | Fresh | 3.8 | −4[a] |
| | 2 $\mu$m | Fresh | 3.6 | 14[b] |

[a] Calculations made using Wenzel equation.

[b] Calculations made using Cassie–Baxter equation. We assume that the contact area between the droplet and air is the half of the whole area of the rough surface.

lotus and colocasia, and 76° and 84° in fagus and magnolia, respectively, the contact angles ($\theta_0$) for the smooth surfaces can be calculated using the Wenzel equation (equation (1)) for microbumps and the Cassie–Baxter equation (equation (3)) for nanobumps. Contact angle ($\Delta\theta$) calculated using $R_f$ on the smooth surface can be found in table 2. It can be seen that the roughness factors and the differences ($\Delta\theta$) between $\theta$ and $\theta_0$ on nanoscale are higher than those in the microscale. This means that nanobumps on the top of a microbump increase contact angle more effectively than microbumps. In the case of hydrophilic leaves, the values of $R_f$ and $\Delta\theta$ change very little on both scales.

Based on the data in figure 11, the coefficient of friction values in the nanoscale are much lower than those in the microscale. It is clearly observed that friction values are scale dependent. The height of a bump and the distance between bumps in microscale is much larger than those in nanoscale, which may be responsible for larger values of friction force on the microscale.

A difference between microbumps and nanobumps for surface enhancement of water repellency is the effect on contact angle hysteresis, in other words, the ease with which a droplet of water can roll on the surface. It has been stated earlier that contact angle hysteresis decreases and contact angle increases due to the decreased contact with the solid surface caused by the air pockets beneath the droplet. The surface

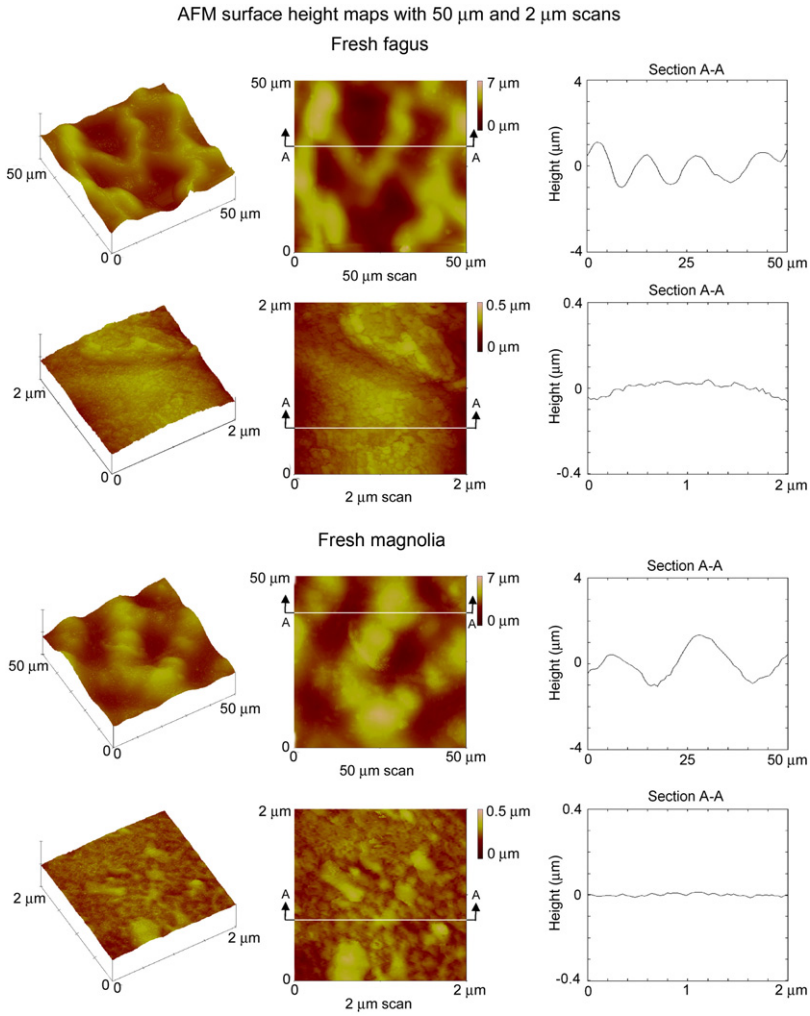


**Figure 10.** Surface height maps and 2D profiles of fagus and magnolia using an AFM in both 50 and 2 $\mu$m scans (Bhushan and Jung 2006).

with nanobumps has high roughness factor compared with that of microbumps. With large distances between microbumps, the probability of air pockets formation decreases, and is responsible for high contact angle hysteresis. Therefore, on the surface with nanobumps, the contact angle is high and contact angle hysteresis is low, and drops rebound easily and can set into a rolling motion with a small tilt angle.

## 5. Micropatterned and nanopatterned surfaces

The next logical step in realizing superhydrophobic surfaces that can be produced is to design surfaces based on understanding of the hydrophobic leaves. By making patterned surfaces, the process of producing 'biomimetic' surfaces has begun, but more experimentation and characterization is necessary. Using methods described previously, the wetting properties of micropatterned and nanopatterned surfaces have been studied and the results are summarized below.

### *5.1. Micropatterned and nanopatterned polymers*

Two types of polymers were used in the study, poly(methyl methacrylate) (PMMA) and polystyrene (PS). PMMA and PS were chosen because they are widely used in MEMS/NEMS devices (Bhushan 2007). Both hydrophilic and hydrophobic surfaces can be produced by using these two polymers, as PMMA has a polar property (hydrophilic) and PS has electrically neutral and nonpolar property (hydrophobic). Furthermore, PMMA structure can be made hydrophobic by coating with a self-assembled monolayer (SAM). For PMMA polymer, four types of surface patterns were fabricated: flat film, low aspect ratio asperities (LAR, 1:1 height-to-diameter ratio), high aspect ratio asperities (HAR, 3:1 height-to-diameter ratio), and lotus pattern (replica from the lotus leaf). For PS polymer, two types of surface patterns were fabricated: flat film and lotus pattern. Figure 12 shows SEM images of the two types of nanopatterned structures, LAR and HAR, and the one type of micropatterned structure, lotus pattern, all on a PMMA surface (Burton and Bhushan 2005, Jung and Bhushan 2006). Both micropatterned and nanopatterned structures were created using soft lithography. For nanopatterned structures, PMMA film was spin coated on the silicon wafer. A UV cured mold (PUA mold) with nanopatterns of interest was made which enables one to create sub-100 nm patterns with high aspect ratio (Choi *et al* 2004). The mold was placed on the

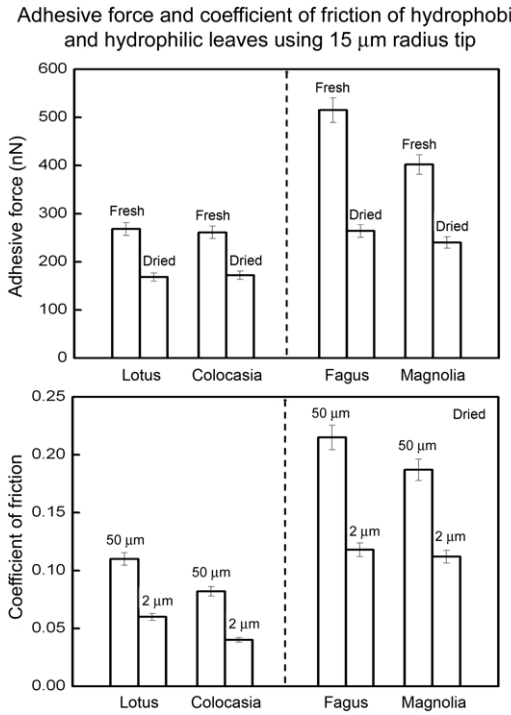


**Figure 11.** Adhesive force for fresh and dried leaves, and the coefficient of friction for dried leaves for 50 $\mu$m and 2 $\mu$m scan sizes for hydrophobic and hydrophilic leaves. All measurements were made using a 15 $\mu$m radius borosilicate tip. Reproducibility for both adhesive force and coefficient of friction is ±5% for all measurements (Bhushan and Jung 2006).

**Table 3.** Roughness factor for micropatterned and nanopatterned polymers (Jung and Bhushan 2006).

| | LAR | HAR | Lotus |
|---|---|---|---|
| $R_f$ | 2.1 | 5.6 | 3.2 |

PMMA film and a slight pressure of ∼10 g cm$^{-2}$ (∼1 kPa) was applied and annealed at 120 °C. Finally, the PUA mold was removed from PMMA film. For micropatterned structures, polydimethylsiloxane (PDMS) mold was first made by casting PDMS against a lotus leaf following by heating. As shown in figure 12, it can be seen that only microstructures exist on the surface of lotus pattern (Yoon 2006).

The PMMA chosen were initially hydrophilic, so to obtain a sample that is hydrophobic, A self-assembled monolayer (SAM) of perfluorodecyltriethoxysilane (PFDTES) was deposited on the sample surfaces using vapor phase deposition technique. PFDTES was chosen because of the hydrophobic nature of the surface. The deposition conditions for PFDTES were 100 °C temperature, 400 Torr pressure, 20 min deposition time, and 20 min annealing time. The polymer surface was exposed to an oxygen plasma treatment (40 W, $O_2$ 187 Torr, 10 s) prior to coating (Bhushan *et al* 2006). The oxygen plasma treatment is necessary to oxidize any organic contaminants on the polymer surface and to also alter the surface chemistry to allow for enhanced bonding between the SAM and the polymer surface.

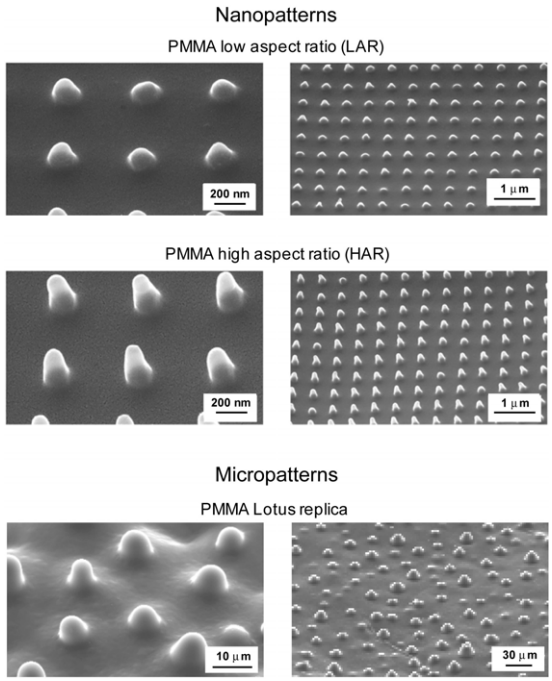


**Figure 12.** Scanning electron micrographs of the two nanopatterned polymer surfaces (shown using two magnifications to see both the asperity shape and the asperity pattern on the surface) and the micropatterned polymer surface (Lotus pattern, which has only microstructures on the surface) (Burton and Bhushan 2005, Jung and Bhushan 2006).

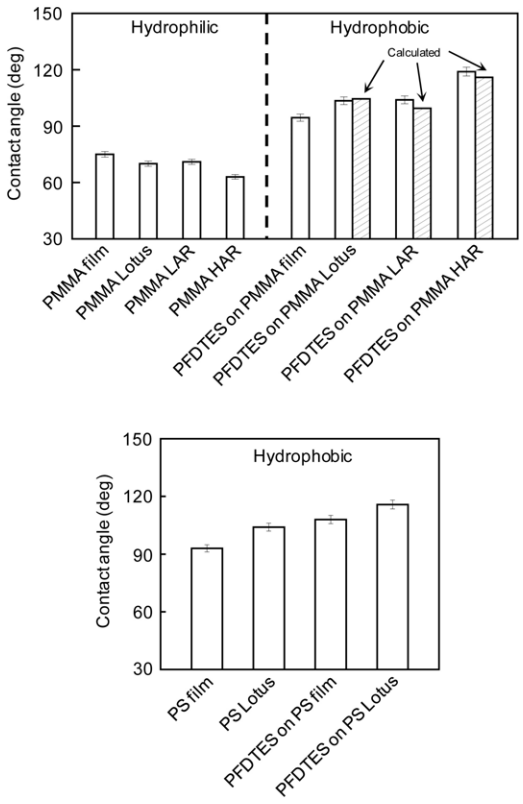


**Figure 13.** Contact angles for various patterned surfaces on PMMA and PS polymers (Jung and Bhushan 2006).

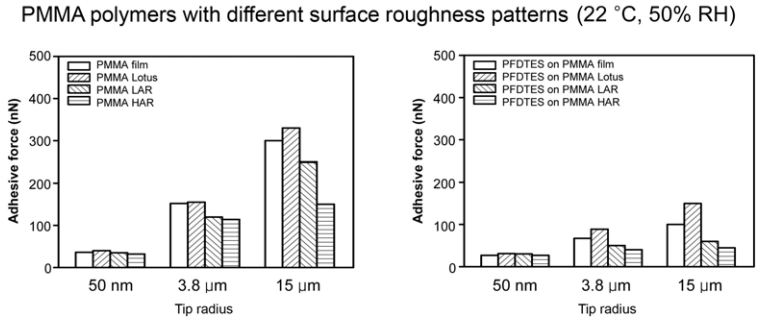


**Figure 14.** Scale-dependent adhesive force for various patterned surfaces measured using AFM tips of various radii (Jung and Bhushan 2006).

*5.1.1. Contact angle measurements.* Jung and Bhushan (2006) conducted the static contact angle measurements on the PMMA and PS materials; see figure 13. Table 3 presents the roughness factor data for various samples. The data show that contact angle of the hydrophilic materials decreases with an increase in the roughness factor, as predicted in figure 1(b). When the polymers were coated with PFDTES, the film surface became hydrophobic. Figure 13 also shows the contact angle data for various PMMA samples coated with PFDTES. For a hydrophobic surface, the model predicts an increase of contact angle with roughness factor, which is what happens in the case of patterned samples. The calculated values of contact angle for various patterned samples based on the contact angle of the smooth film and Wenzel equation are also presented. The measured contact angle values for the lotus pattern were comparable to the calculated values whereas for the LAR and HAR patterns, they are higher. It suggests that nanopatterns benefit from air pocket formation. For the PS material, the contact angle of the lotus pattern also increased with increased roughness factor.

*5.1.2. Scale dependence on adhesive force.* Scale-dependent effects of adhesion and friction are present because the tip/surface interface changes with size. Meniscus force will change by varying either the tip radius, the hydrophobicity of the sample, or the number of contact and near-contacting points. Figure 14 shows the dependence of tip radius and hydrophobicity on adhesive force for PMMA and PFDTES coated on PMMA (Jung and Bhushan 2006). When the radius of the tip is changed, the contact angle of the sample is changed, and asperities are added to the sample surface, the adhesive force will change due to the change in the meniscus force and the real area of contact.

The two plots in figure 14 show the adhesive force on a linear scale for the different surfaces with varying tip radius. The left bar chart in figure 14 is for hydrophilic PMMA film, Lotus pattern, LAR, and HAR, and shows the effect of tip radius and hydrophobicity on adhesive force. For increasing radius, the adhesive force increases for each material. With a larger radius, the real area of contact and the meniscus contribution increase, resulting in the increased adhesion. The right bar chart in figure 14 shows the results for PFDTES coated on each material. These samples show the same trends as the film samples, but the increase in adhesion is not as dramatic. The hydrophobicity of PFDTES on material reduces meniscus forces, which in turn reduces adhesion from the surface. The dominant mechanism for the hydrophobic material is real area of contact and not meniscus force, whereas with hydrophilic material there is a combination of real area of contact and meniscus forces.

### *5.2. Micropatterned Si surfaces*

Single-crystal silicon (Si) was used in the study. Silicon material has traditionally been the most commonly used structural material for micro/nanocomponents (Bhushan 2007). Hydrophilic surfaces can be produced by using silicon material. The Si surface can be made hydrophobic by coating with a self-assembled monolayer (SAM). One of purpose of this study was to study the transition for Cassie and Baxter regime to Wenzel regime by changing the distance between the pillars. To create patterned Si, two series of nine samples each were fabricated using photolithography (Barbieri *et al* 2007). Series 1 has 5 $\mu$m diameter and 10 $\mu$m height flat-top, cylindrical pillars with different pitch values (7, 7.5, 10, 12.5, 25, 37.5, 45, 60, and 75 $\mu$m), and series 2 has 14 $\mu$m diameter and 30 $\mu$m height flat-top, cylindrical pillars with different pitch values (21, 23, 26, 35, 70, 105, 126, 168, and 210 $\mu$m). The pitch is the spacing between the centers of two adjacent pillars. The Si chosen were initially hydrophilic, so to obtain a sample that is hydrophobic, a SAM of 1, 1,-2, 2,-tetrahydroperfluorodecyltrichlorosilane ($PF_3$) was deposited on the sample surfaces using vapor phase deposition technique (Barbieri *et al* 2007). $PF_3$ was chosen because of the hydrophobic nature of the surface. The thickness and rms roughness of the SAM of $PF_3$ were 1.8 and 0.14 nm, respectively (Kasai *et al* 2005).

An optical profiler was used to measure the surface topography of the patterned surfaces (Bhushan and Jung 2007, Jung and Bhushan 2008). One sample each from the two series was chosen to characterize the surfaces. Two different surface height maps can be seen for the patterned Si in figure 15. In each case, a 3D map and a flat map along with a 2D profile in a given location of the flat 3D map are shown. A scan size of 100 $\mu$m $\times$ 90 $\mu$m was used to obtain a sufficient amount of pillars to characterize the surface but also to maintain enough resolution to get an accurate measurement.

The images found with the optical profiler indicate that the flat-top, cylindrical pillars on the Si surface are distributed on the entire surface. These pillars were distributed in a square

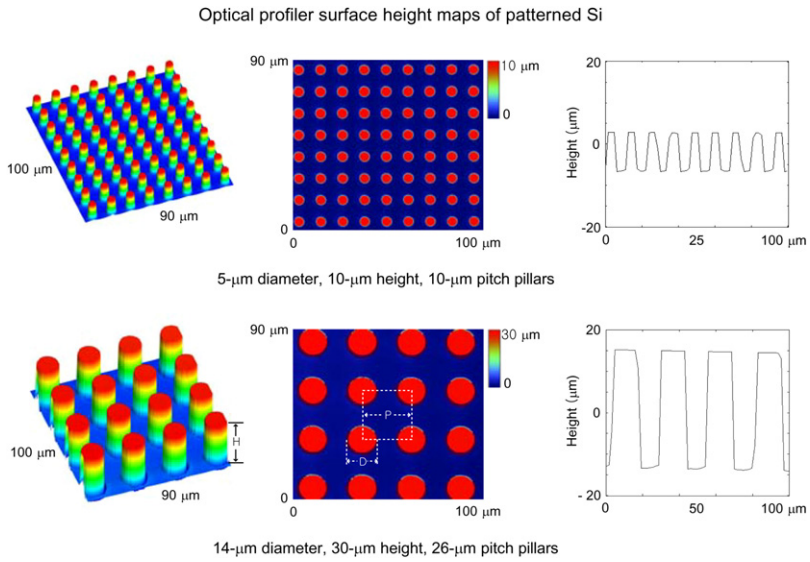


**Figure 15.** Surface height maps and 2D profiles of the patterned surfaces using an optical profiler. (Bhushan and Jung 2007).

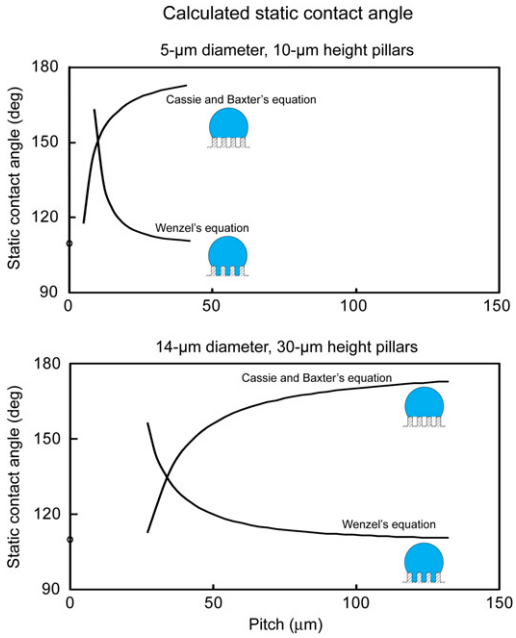


**Figure 16.** Calculated static contact angle as a function of geometric parameters for a given value of $\theta_0$ using Wenzel and Cassie and Baxter equations for two series of the patterned surfaces with different pitch values (Bhushan and Jung 2007).

grid with different pitch values. Each sample series has the same series of roughness factors as a ratio of the solid–liquid area to its projected area on a flat surface (roughness factor $= 1+\pi DH/P^2$). Keeping roughness factors constant means that Cassie and Baxter's and Wenzel's theoretical models predict exactly the same series of contact angle values for all two series of nine samples.

*5.2.1. Contact angle relationships for a geometry of flat-top, cylindrical pillars.* To show an application example of Wenzel and Cassie and Baxter equations, let us consider a geometry of flat-top, cylindrical pillars of diameter $D$, height $H$, and pitch $P$ distributed in a regular square array as shown in figure 15. For the special case where the droplet size is much larger than $P$ (of interest in this study), a droplet only contacts the flat top of the pillars in the composite interface, and the cavities are filled with air. For this case, $f_{\mathrm{LA}} = 1 - \frac{\pi D^2}{4P^2} = 1 - f_{\mathrm{SL}}$. Let us further assume that the flat tops are smooth with $R_{\mathrm{f}} = 1$. Equations (1) and (3) for this case reduce to (Bhushan and Jung 2007)

$$\text{Wenzel: } \cos\theta = \left(1 + \frac{\pi DH}{P^2}\right)\cos\theta_0 \tag{8}$$

$$\text{Cassie and Baxter: } \cos\theta = \frac{\pi D^2}{4P^2}(\cos\theta_0 + 1) - 1. \tag{9}$$

Geometrical values of the flat-top, cylindrical pillars in series 1 and 2 are used for calculating the contact angle for the above-mentioned two cases. Figure 16 shows the plot of the predicted values of the contact angle as a function of pitch between the pillars for the two cases. Wenzel's and Cassie and Baxter's equations present two possible equilibrium states for a water droplet on the surface. This indicates that there is a critical pitch below which the composite interface dominates and above which the homogeneous interface dominates the wetting behavior. The process to design the superhydrophobic surfaces is important in determining the equilibrium water droplet. Therefore, one needs to find the critical point that can be used to design the superhydrophobic surfaces. It should also be noted that even in cases where the liquid droplet does not contact the bottom of the cavities, the water droplet in a metastable state becomes unstable and the transition from Cassie and Baxter regime to Wenzel regime occurs if the pitch is large.

*5.2.2. Transition criterion.* A stable composite interface is essential for the successful design of superhydrophobic

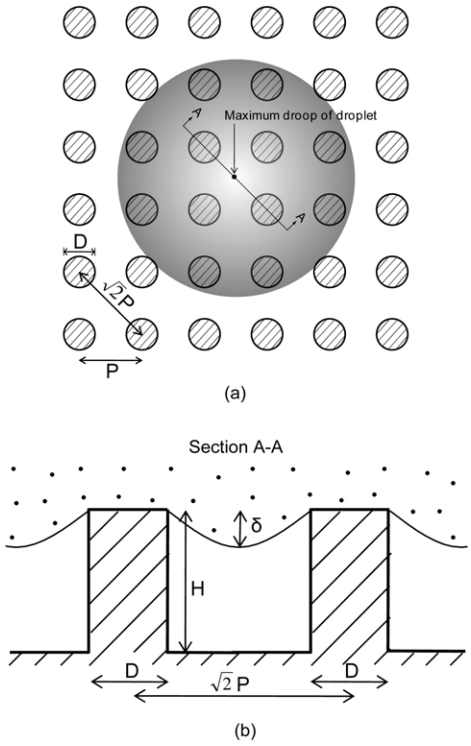


**Figure 17.** A small water droplet suspended on a superhydrophobic surface consisting of a regular array of circular pillars. (a) Plan view. The maximum droop of droplet occurs in the center of square formed by four pillars. (b) Side view in section A–A. The maximum droop of droplet ($\delta$) can be found in the middle of two pillars which are diagonally across (Jung and Bhushan 2007, 2008).

surfaces. However, the composite interface is fragile and it may transform into the homogeneous interface. Nosonovsky and Bhushan (2007a) have studied destabilizing factors for the composite interface and found that the sign of the surface curvature is important, especially in the case of multiscale (hierarchical) roughness. A convex surface (with bumps) leads to a stable interface and high contact angle. Also, they have been suggested the effects of droplet's weight and curvature among the factors which affect the transition.

Bhushan and Jung (2007) and Jung and Bhushan (2007, 2008) developed the model to predict the transition from Cassie and Baxter regime to Wenzel regime based on the factors discussed above. First, they considered a small water droplet suspended on a superhydrophobic surface consisting of a regular array of circular pillars with diameter $D$, height $H$, and pitch $P$ as shown in figure 17. The local deformation for small droplets is governed by surface effects rather than gravity. The curvature of a droplet is governed by the Laplace equation, which relates the pressure inside the droplet to its curvature (Adamson 1990). The curvature is the same at the top and at the bottom of the droplet (Lafuma and Quéré 2003, Nosonovsky and Bhushan 2007b). For the patterned surface considered here, the maximum droop of the droplet occurs in the center of the square formed by the four pillars as shown in figure 17(a). Therefore, the maximum droop of the droplet ($\delta$) in the recessed region can be found in the middle of two pillars which are diagonally across as shown in figure 17(b), which is $(\sqrt{2}P - D)^2/(8R)$. If the droop is much greater than the depth of the cavity,

$$(\sqrt{2}P - D)^2/R \geqslant H \tag{10}$$

then the droplet will just contact the bottom of the cavities between pillars, resulting into the transition from Cassie and Baxter regime to Wenzel regime. Furthermore, in the case of large distances between the pillars, the liquid–air interface can easily be destabilized due to dynamic effects, such as surface waves which are formed at the liquid–air interface due to the gravitational or capillary forces. This leads to the formation of the homogeneous solid–liquid interface.

*5.2.3. Contact angle measurements.* The initial experiment performed with 1 mm in radius (5 $\mu$l volume) on the patterned Si coated with $PF_3$ was to determine the static contact angle (Bhushan and Jung 2007, Jung and Bhushan 2007, 2008). The contact angles on the prepared surfaces are plotted as a function of pitch between the pillars in figure 18(a). A dotted line represents the transition criteria range obtained using equation (10). The flat Si coated with $PF_3$ showed the static contact angle of 109°. As the pitch increases up to 45 $\mu$m of series 1 and 126 $\mu$m of series 2, the static contact angle first increases gradually from 152° to 170°. Then, the contact angle starts decreasing sharply. Initial increase with an increase of pitch has to do with more open air space present which increases the propensity of air pocket formation. As predicted from the transition criteria (equation (10)), the decrease in contact angle at higher pitch values results due to the transition from composite interface to solid–liquid interface. In the series 1, the value predicted from the transition criteria is a little higher than the experimental observations. However, in the series 2, there is a good agreement between the experimental data and the theoretically predicted values for the transition from Cassie and Baxter regime to Wenzel regime.

Figure 18(b) shows hysteresis and tilt angle as a function of pitch between the pillars (Bhushan and Jung 2007). The flat Si coated with $PF_3$ showed a hysteresis angle of 34° and tilt angle of 37°. The patterned surfaces with low pitch increase the hysteresis and tilt angles compared to the flat surface due to the effect of sharp edges on the pillars, resulting into pinning (Nosonovsky and Bhushan 2005). Hysteresis for a flat surface can arise from roughness and surface heterogeneity. For a droplet moving down on the inclined patterned surfaces, the line of contact of the solid, liquid and air will be pinned at the edge point until it will be able to move, resulting into increasing hysteresis and tilt angles. Figure 19 shows droplets on patterned Si with 5 $\mu$m diameter and 10 $\mu$m height pillars with different pitch values. The asymmetrical shape of the droplet signifies pinning. The pinning on the patterned surfaces can be observed as compared to the flat surface. The patterned surface with low pitch (7 $\mu$m) has more the pinning than the patterned surface with high pitch (37.5 $\mu$m), because the patterned surface with low pitch has more sharp edges contacting with a droplet.

For various pitch values, hysteresis and tilt angles show the same trends with varying pitch between the pillars. After an initial increase as discussed above, they gradually decrease

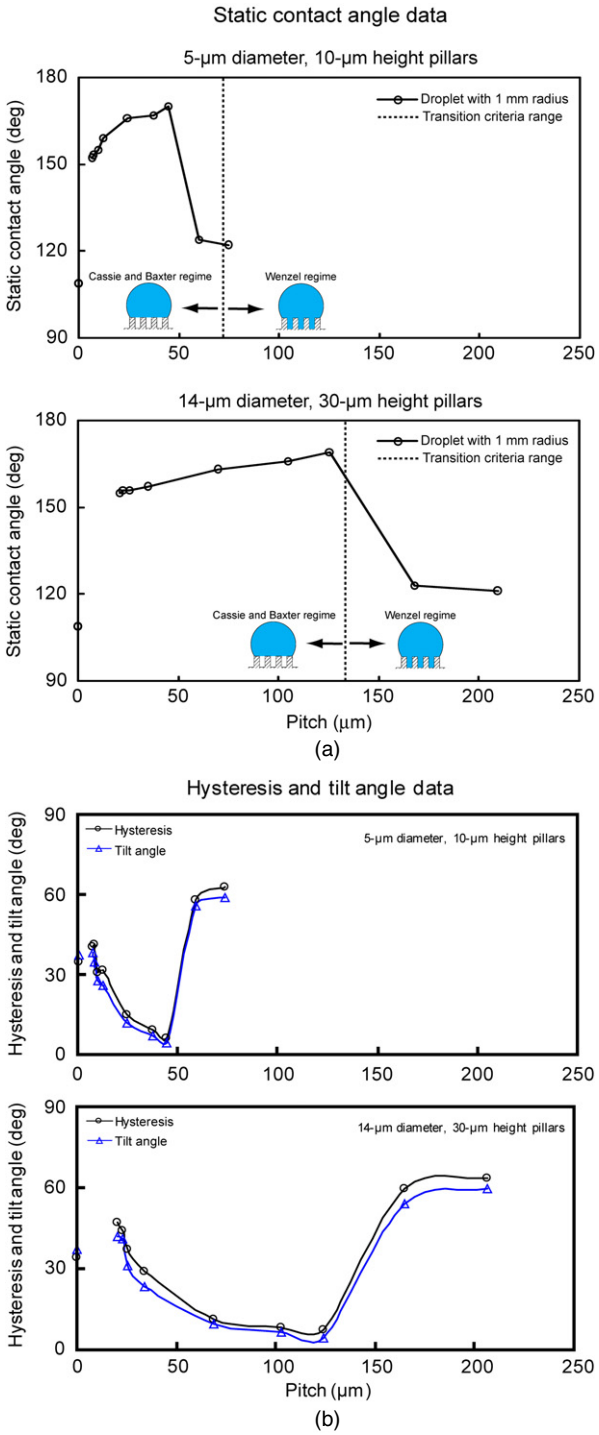


**Figure 18.** (a) Static contact angle (a dotted line represents the transition criteria range obtained using equation (10)) and (b) hysteresis and tilt angles as a function of geometric parameters for two series of the patterned surfaces with different pitch values for a droplet with 1 mm in radius (5 $\mu$l volume). Data at zero pitch correspond to a flat sample (Bhushan and Jung 2007, Jung and Bhushan 2008).

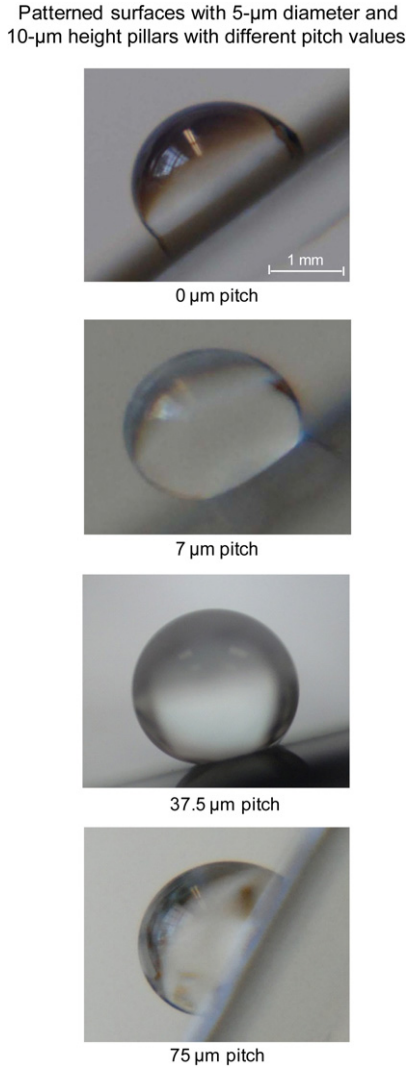


**Figure 19.** Optical micrographs of droplets on the inclined patterned surfaces with different pitch values. The images were taken when the droplet started to move down. Data at zero pitch correspond to a flat sample (Bhushan and Jung 2007).

with increasing pitch (due to reduced number of sharp edges) and show an abrupt minimum in the value which has the highest contact angle. The lowest hysteresis and tilt angles are 5° and 3°, respectively, which were observed on the patterned Si with 45 $\mu$m of series 1 and 126 $\mu$m of series 2. As discussed earlier, an increase in the pitch value allows the formation of composite interface. At higher pitch values, it is difficult to form the composite interface. The decrease in hysteresis and tilt angles occurs due to formation of composite interface at pitch values raging from 7 to 45 $\mu$m in series 1 and from 21 to 126 $\mu$m in series 2. The hysteresis and tilt angles start to increase again due to lack of formation of air pockets at pitch values raging from 60 to 75 $\mu$m in series 1 and from 168 to 210 $\mu$m in series 2. These results suggest that the air pocket formation and the reduction of pinning in the patterned surface play an important role for a surface with both low hysteresis and tilt angle (Bhushan and Jung 2007). Hence, to create superhydrophobic surfaces, it is important that they are able to form a stable composite interface with air pockets between solid and liquid. Capillary waves, nanodroplet condensation, hydrophilic spots due to chemical surface inhomogeneity, and liquid pressure can destroy the composite interface. Nosonovsky and Bhushan (2007a, 2007b, 2007d) suggested

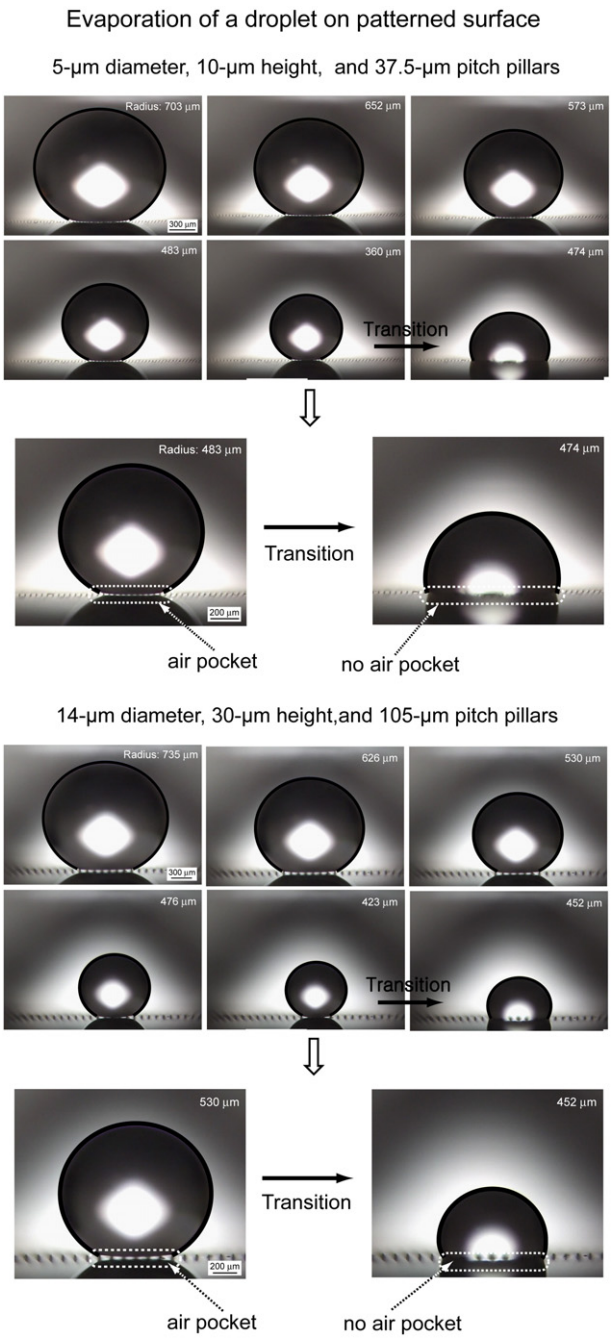


**Figure 20.** Evaporation of a droplet on two different patterned surfaces. The initial radius of the droplet is about 700 $\mu$m, and the time interval between successive photos is 30 s. As the radius of droplet reaches 360 $\mu$m on the surface with 5 $\mu$m diameter, 10 $\mu$m height, and 37.5 $\mu$m pitch pillars, and 420 $\mu$m on the surface with 14 $\mu$m diameter, 30 $\mu$m height, and 105 $\mu$m pitch pillars, the transition from Cassie and Baxter regime to Wenzel regime occurs, as indicated by the arrow. Before the transition, air pocket is clearly visible at the bottom area of the droplet, but after the transition, air pocket is not found at the bottom area of the droplet (Jung and Bhushan 2008).

that these factors which make the composite interface unstable have different characteristic length scales, so nanostructures or the combination of microstructures and nanostructures is required to resist them.

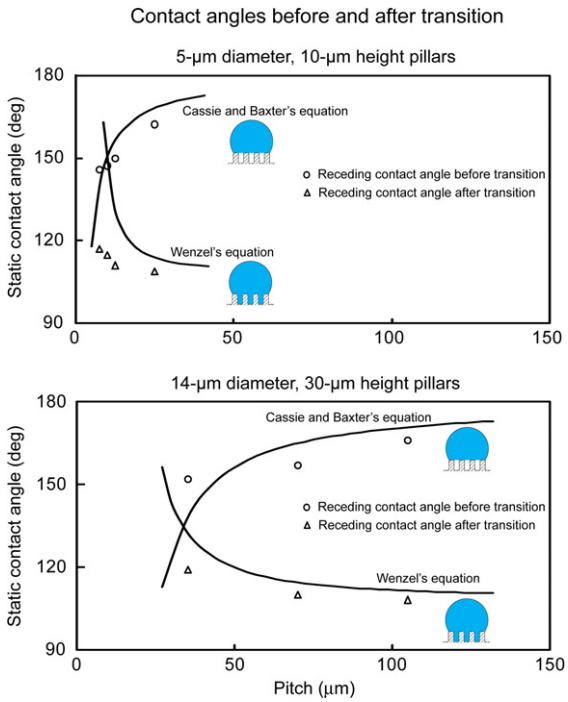


**Figure 21.** Receding contact angle as a function of geometric parameters before (circle) and after (triangle) transition compared with predicted static contact angle values obtained using Wenzel and Cassie and Baxter equations (solid lines) with a given value of $\theta_0$ for two series of the patterned surfaces with different pitch values (Jung and Bhushan 2008).

*5.2.4. Observation of transition during the droplet evaporation.* Jung and Bhushan (2007, 2008) performed the droplet evaporation experiments to observe the transition from Cassie and Baxter regime to Wenzel regime on two different patterned Si surfaces coated with $PF_3$. The series of six images in figure 20 show the successive photos of a droplet evaporating on two patterned surfaces. The initial radius of the droplet is about 700 $\mu$m, and the time interval between successive photos is 30 s. In the first five photos, the drop is first in a hydrophobic state, and its size gradually decreases with time. However, as the radius of the droplet reaches 360 $\mu$m on the surface with 5 $\mu$m diameter, 10 $\mu$m height, and 37.5 $\mu$m pitch pillars, and 423 $\mu$m on the surface with 14 $\mu$m diameter, 30 $\mu$m height, and 105 $\mu$m pitch pillars, the transition from Cassie and Baxter regime to Wenzel regime occurs, as indicated by the arrow. Figure 20 also shows a zoom-in of water droplets on two different patterned Si surfaces coated with $PF_3$ before and after the transition. The light passes below the left droplet, indicating that air pockets exist, so that the droplet is in Cassie and Baxter state. However, an air pocket is not visible below the bottom right droplet, so it is in Wenzel state. This could result from an impalement of the droplet in the patterned surface, characterized by a smaller contact angle.

To verify the contact angle before and after transition, the values of the contact angle are plotted against the theoretically predicted value, based on the Wenzel (calculated using equation (1)) and Cassie and Baxter (calculated using equation (3)) models. Figure 21 shows the static contact angle

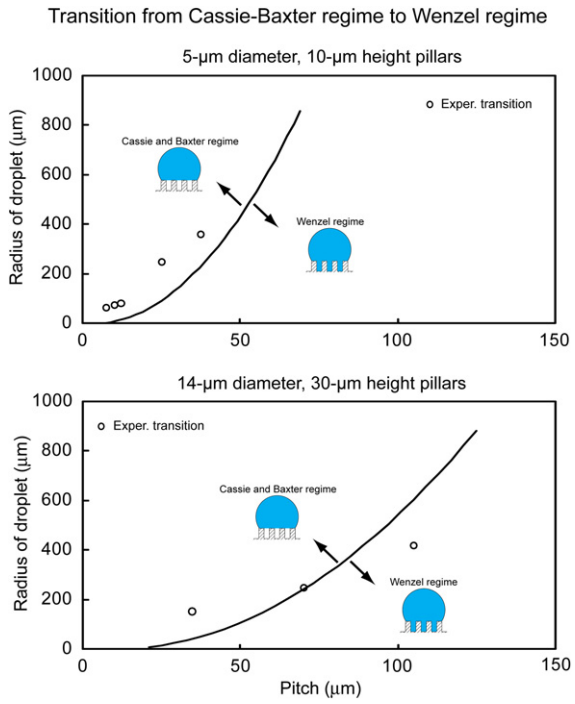


**Figure 22.** Radius of droplet as a function of geometric parameters for the experimental results (circle) compared with the transition criteria from Cassie and Baxter regime to Wenzel regime (solid lines) for two series of the patterned surfaces with different pitch values (Jung and Bhushan 2008).

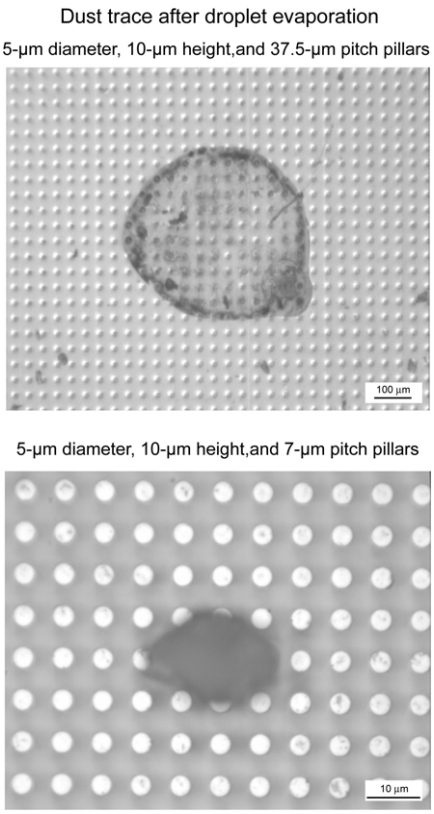


**Figure 23.** Dust trace remained after droplet evaporation for the patterned surface. In the top image, the transition occurred at 360 $\mu$m radius of droplet, and in the bottom image, the transition occurred at about 20 $\mu$m radius of droplet during the process of droplet evaporation. The footprint size is about 450 and 25 $\mu$m for the top and bottom images, respectively (Jung and Bhushan 2008).

as a function of geometric parameters for the experimental contact angles before (circle) and after (triangle) the transition compared with Wenzel and Cassie and Baxter equations (solid lines) with a given value of $\theta_0$ for two series of the patterned Si with different pitch values coated with $PF_3$ (Jung and Bhushan 2008). The fit is good between the experimental data and the theoretically predicted values for the contact angles before and after transition.

To prove the validity of the transition criteria in terms of droplet size, the critical radius of droplet deposited on the patterned Si with different pitch values coated with $PF_3$ is measured during the evaporation experiment (Jung and Bhushan 2007, 2008). Figure 22 shows the radius of a droplet as a function of geometric parameters for the experimental results (circle) compared with the transition criteria from Cassie and Baxter regime to Wenzel regime (solid lines) for two series of the patterned Si with different pitch values coated with $PF_3$. It is found that the critical radius of impalement is indeed in good quantitative agreement with our predictions. The critical radius of the droplet increases linearly with the geometric parameter (pitch). For the surface with small pitch, the critical radius of droplet can become quite small. Based on this trend, one can design superhydrophobic surfaces, even for small droplets.

To verify the transition, Jung and Bhushan (2007, 2008) used another approach using the dust mixed in water. Figure 23 presents the dust trace remaining after droplet with 1 mm radius (5 $\mu$l volume) evaporation on the patterned Si surface with pillars of 5 $\mu$m diameter and 10 $\mu$m height with 37.5 $\mu$m pitch in which the transition occurred at 360 $\mu$m radius of the droplet, and with 7 $\mu$m pitch in which the transition occurred at about 20 $\mu$m radius of the droplet during the process of evaporation. As shown in the top image, after the transition from Cassie and Baxter regime to Wenzel regime, the dust particles remained not only at the top of the pillars but also at the bottom with a footprint size of about 450 $\mu$m. However, as shown in the bottom image, the dust particles remained on only a few pillars until the end of the evaporation process. The transition occurred at about 20 $\mu$m radius of droplet and the dust particles left a footprint of about 25 $\mu$m. From figure 22, it is observed that the transition occurs at about 300 $\mu$m radius of droplet on the 5 $\mu$m diameter and 10 $\mu$m height pillars with 37.5 $\mu$m pitch, but the transition does not occur on the patterned Si surface with pitch of less than about 5 $\mu$m. These experimental observations are consistent with model predictions. In the literature, it has been shown that on superhydrophobic natural lotus, the droplet remains almost in Cassie and Baxter regime during the evaporation process (Zhang *et al* 2006). This indicates that the distance between the pillars should be minimized enough to improve the ability of the droplet to resist sinking.

*5.2.5. Observation and measurement of contact angle using ESEM.* Figure 24 shows how water droplets grow and merge

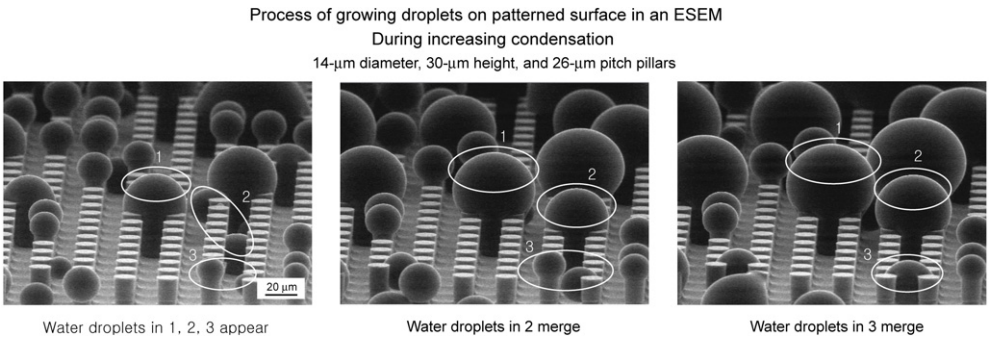


**Figure 24.** Microdroplet (in dimension of less than 1 mm diameter) growing and merging process under ESEM during increasing condensation by decreasing temperature. Left image: some small water droplets appear at the beginning, i.e. water droplets 1, 2, 3. Middle image: water droplets at locations 1 and 3 increase in size and water droplets at location 2 merge together to form one big droplet. Right image: water droplets at locations 1 and 2 increase in size and water droplets at location 3 merge together to form one big droplet (Jung and Bhushan 2008).

under ESEM (Jung and Bhushan 2008). ESEM is used as a contact angle analysis tool to investigate superhydrophobicity on the patterned surfaces. Microdroplets (in dimension of less than 1 mm diameter) are distributed on the patterned surface coated with $PF_3$ during increasing condensation by decreasing temperature. Even if the microdroplets are not the same size, they show the hydrophobic characteristics of the patterned surface. At the beginning, some small water droplets appear, i.e. water droplets at locations 1, 2 and 3 in the left image. During increasing condensation by decreasing temperature, water droplets at locations 1 and 3 gradually increase in size and water droplets at location 2 merge together to form one big droplet in the middle image. With further condensation, water droplets at locations 1 and 2 increase in size and water droplets at location 3 merge together to one big droplet in right image. In all cases condensation was initiated at the bottom, therefore, as can be observed, the droplets are in the Wenzel regime. This could also be evidence that the droplet on the macroscale used in the conventional contact angle measurement comes from the merging of smaller droplets.

Compared with the conventional contact angle measurement, ESEM is able to provide detailed information about the contact angle of microdroplets on patterned surfaces. The diameter of the water droplets used for the contact angle measurement is more than 10 $\mu$m such that the size limit pointed out by Stelmashenko *et al* (2001) was avoided. For droplet size less than 1 $\mu$m, substrate backscattering can distort the intensity profile such that the images are inaccurate.

As shown in figure 25, the static contact angle and hysteresis angle of the microdroplets condensed on flat and two different patterned surfaces were obtained from the images and corrected using methodology mentioned earlier. The difference between the data estimated from the images and corrected $\theta$ is about 3%. Once the microdroplet's condensation and evaporation has reached a dynamic equilibrium, static contact angles are determined. The flat Si coated with $PF_3$ showed a static contact angle of 98°. The patterned surfaces coated with $PF_3$ increase the static contact angle compared to the flat surface coated with $PF_3$ due to the effect of roughness. Advancing contact angle was taken after increasing condensation by decreasing the temperature of the cooling stage. Receding contact angle was taken after increasing evaporation by increasing the temperature of the cooling stage. The hysteresis angle was then calculated (Jung and Bhushan 2008).

Figure 26 shows hysteresis angle as a function of geometric parameters for the microdroplets formed in the ESEM (triangle) for two series of the patterned Si with different pitch values coated with $PF_3$. Data at zero pitch correspond to a flat Si sample. The droplets with about 20 $\mu$m radii which are larger than the pitch were selected in order to look at the effect of pillars in contact with the droplet. This data were compared with conventional contact angle measurements obtained with the droplet with 1 mm radius (5 $\mu$l volume) (circle and solid lines) (Bhushan and Jung 2007). When the distance between pillars increases above a certain value, the contact area between the patterned surface and the droplet decreases, resulting in the decrease of the hysteresis angle. Both the droplets with 1 mm and 20 $\mu$m radii show the same trend. The hysteresis angles for the patterned surfaces with low pitch are higher compared to the flat surface due to the effect of sharp edges on the pillars, resulting in pinning (Nosonovsky and Bhushan 2005). Hysteresis for a flat surface can arise from roughness and surface heterogeneity. For a droplet advancing forward on the patterned surfaces, the line of contact of the solid, liquid and air will be pinned at the edge point until it is able to move, resulting in increasing hysteresis angle. The hysteresis angle for the microdroplet from ESEM is lower as compared to that for the droplet with 1 mm radius. The difference of hysteresis angle between a microdroplet and a droplet with 1 mm radius could come from the different pinning effects, because the latter has more sharp edges contacting with a droplet compared with the former. The results show how droplet size can affect the wetting properties of patterned Si surfaces.

## 6. Need of hierarchical roughness for superhydrophobicity

The mechanism of roughness-induced hydrophobicity is complicated and involves effects at various scale ranges

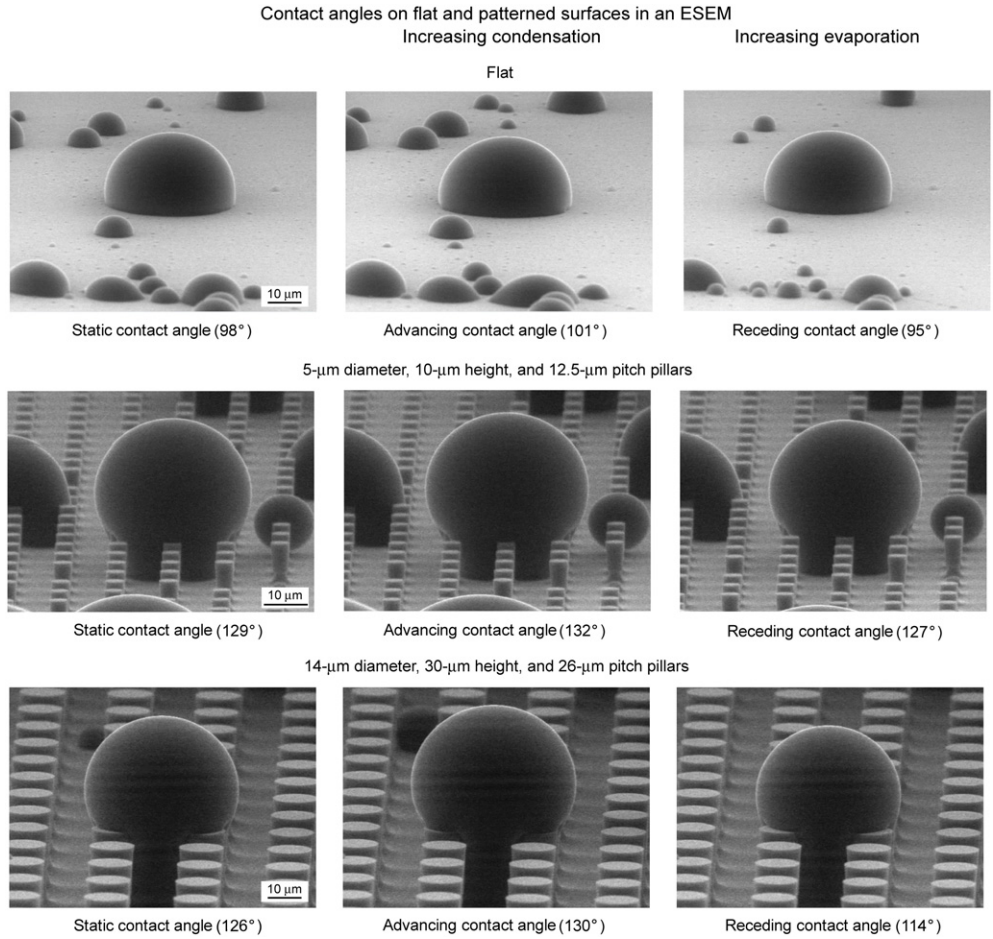


**Figure 25.** Microdroplets on flat and two patterned surfaces using ESEM. Second set of images were taken during increasing condensation, and the third set of images were taken during increasing evaporation. Static contact angle was measured when the droplet was stable. Advancing contact angle was measured after increasing condensation by decreasing the temperature of the cooling stage. Receding contact angle was measured after decreasing evaporation by increasing the temperature of the cooling stage (Jung and Bhushan 2008).

(Nosonovsky and Bhushan 2007a, 2007b, 2007c, 2007d, 2008). For most superhydrophobic surfaces, it is important that composite solid–air–liquid interface is formed. A composite interface dramatically decreases the area of contact between liquid and solid and, therefore, decreases adhesion of a liquid droplet to the solid surface and contact angle hysteresis. Formation of a composite interface is a multiscale phenomenon, which depends upon relative sizes of the liquid droplets and roughness details. The transition from a composite interface to a homogeneous interface is irreversible, therefore, stability of a composite interface is crucial for superhydrophobicity and should be addressed for successful development of superhydrophobic surfaces. Nosonovsky and Bhushan (2007a, 2007b, 2007d, 2008) have demonstrated that a multiscale (hierarchical) roughness can help to resist the destabilization, with convex surfaces pinning the interface and thus leading to stable equilibrium as well as preventing from filling the gaps between the pillars even in the case of a hydrophilic material. Such multiscale roughness has been found in natural and successful artificial superhydrophobic surfaces.

The structure of ideal hierarchical surface is shown in figure 27. Based on the proposed transition criteria in the paper, for a structure with circular pillars, the following relationship should hold for a composite interface, $(\sqrt{2}P - D)^2/R < H$, equation (10). As an example, for a droplet with a radius on the order of 1 mm or larger, a value of $H$ on the order of 30 $\mu$m, $D$ on the order of 15 $\mu$m, a $P$ on the order of 130 $\mu$m (figure 18) is optimum. Nanoasperities can pin the liquid–air interface and thus prevent liquid from filling the valleys between asperities. They are also required to support nanodroplets, which may condense in the valleys between large asperities. Therefore, nanoasperities should have a small pitch to handle nanodroplets, less than 1 mm down to few nm radius. The values of $h$ on the order of 10 nm and $d$ on the order of 100 nm can be easily fabricated.

## 7. Summary

Hydrophobicity, as well as low adhesion and friction, is desirable for many industrial applications. Hydrophobic leaves, such as those of lotus and colocasia, provide perfect samples to learn from and in turn apply these principles in designing superhydrophobic surfaces. Introducing patterned roughness, similar to that found on leaves, is the first step in

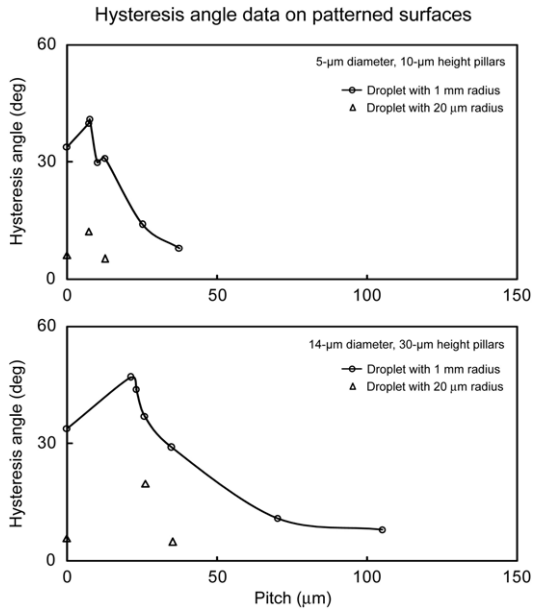


**Figure 26.** Hysteresis angle as a function of geometric parameters for the microdroplet with about 20 $\mu$m radius from ESEM (triangle) compared with the droplet with 1 mm radius (5 $\mu$l volume) (circle and solid lines) for two series of the patterned surfaces with different pitch values. Data at zero pitch correspond to a flat sample (Jung and Bhushan 2008).

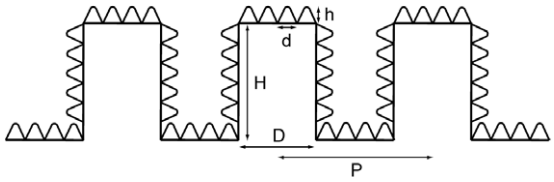


**Figure 27.** Schematic of structure of an ideal hierarchical surface. Microasperities consist of the circular pillars with diameter $D$, height $H$, and pitch $P$. Nanoasperities consist of pyramidal nanoasperities of height $h$ and diameter $d$ with rounded tops.

realizing 'biomimetic' surfaces that can be applied to other industrial applications.

By analyzing surface roughness, adhesion and friction data for hydrophobic and hydrophilic leaves on the microscale and nanoscale, the factors to create hydrophobic surfaces have been identified. After attempting to remove the surface layer, it was found that no wax exists on the hydrophilic leaves but a thin wax film exists on the hydrophobic leaves. The combination of wax and roughness of the leaf is what creates a superhydrophobic surface. Roughness factors of nanobumps are much larger than those of microbumps and presence of nanobumps is responsible for the increase in contact angle for hydrophobic surfaces. Adhesion force and the coefficient of friction have also been measured to characterize the surface of the leaves. The adhesive force decreases from fresh leaves to dried leaves due to decrease in the moisture after the leaves have dried. The adhesive force of the hydrophilic leaves is higher than that of the hydrophobic leaves because of a higher real area of contact between the tip and leaf sample, which also results in higher friction force. The experimental results also show that the coefficient of friction is dependent on the scan size. The height of a bump and the distance between bumps in microscale is much larger than those in nanoscale, which may be responsible for larger values of friction force on the microscale.

Results for the micropatterned and nanopatterned polymer samples were similar to those found for hydrophobic and hydrophilic leaves. Increasing roughness on a hydrophilic surface decreases the contact angle, whereas increasing roughness on a hydrophobic surface increases contact angle. The micropatterned surface has a higher roughness factor than nanopatterned surface, but with similar contact angle. It suggests that nanopatterns benefit from air pocket formation. For hydrophilic materials, with increasing tip radius, the adhesive force increases due to increased real area of contact between the tip and the surface and meniscus force contributions, whereas for hydrophobic materials the adhesive force increases due to increased real area of contact and not meniscus force.

A criterion was developed to predict the transition from Cassie and Baxter regime to Wenzel regime, considering water droplet size as a parameter on the patterned surfaces with various distributions of geometrical parameters. For a droplet of fixed volume, the experimental observations showed that there is a good agreement between the experimental data and the theoretically predicted transition on patterned surfaces with varying pitch values. In addition, in evaporation experiment where the droplet size varied, the experimentally observed critical radius of droplet is in good quantitative agreement with our proposed criterion. As the distance between pillars on the surface was reduced with respect to a droplet size, the droplet remains at the top of the pillars during the whole evaporation process, resulting into a strong superhydrophobic surface even for droplet sizes comparable to the distance between pillars. This indicates that the distance between the pillars should be reduced enough to improve the ability of the droplet to resist sinking.

ESEM was used as a contact angle analysis tool to investigate superhydrophobicity on the patterned surfaces. Compared with the conventional contact angle measurement, ESEM is able to provide insight into the formation of microdroplet and detailed information about the contact angle on the patterned surfaces. From observations of wetting behavior using ESEM, hysteresis angles for the microdroplet with about 20 $\mu$m radius showed the same trends with those for the droplet with 1 mm radius. When the distance between pillars increases, the contact area between the patterned surface and the droplet decreases, resulting in the decrease of the hysteresis angle. ESEM has been shown to be a useful tool for characterizing the superhydrophobicity of the patterned surface.

Hierarchical roughness can help to resist the destabilization with convex surfaces by pinning the interface and thus leading to stable equilibrium as well as preventing from filling the gaps between the pillars even in the case of hydrophilic material. A structure of ideal hierarchical surface was suggested for superhydrophobicity.

## References


Adamson A V 1990 *Physical Chemistry of Surfaces* (New York: Wiley)

Barbieri L, Wagner E and Hoffmann P 2007 Water wetting transition parameters of perfluorinated substrates with periodically distributed flat-top microscale obstacles *Langmuir* **23** 1723–34

Barthlott W and Neinhuis C 1997 Purity of the sacred lotus, or escape from contamination in biological surfaces *Planta* **202** 1–8

Bartolo D, Bouamrirene F, Verneuil E, Buguin A, Silberzan P and Moulinet S 2006 Bouncing or sticky droplets: impalement transitions on superhydrophobic micropatterned surfaces *Europhys. Lett.* **74** 299–305

Bhushan B 1999 *Handbook of Micro/Nanotribology* 2nd edn (Boca Raton, FL: CRC Press)

Bhushan B 2002 *Introduction to Tribology* (New York: Wiley)

Bhushan B 2003 Adhesion and stiction: mechanisms, measurement techniques and methods for reduction *J. Vac. Sci. Technol.* B **21** 2262–96

Bhushan B 2005 *Nanotribology and Nanomechanics—An Introduction* (Heidelberg: Springer)

Bhushan B 2007 *Springer Handbook of Nanotechnology* 2nd edn (Heidelberg: Springer)

Bhushan B, Hansford D and Lee K K 2006 Surface modification of silicon and polydimethylsiloxane surfaces with vapor-phase-deposited ultrathin fluorosilane films for biomedical nanodevices *J. Vac. Sci. Technol.* A **24** 1197–202

Bhushan B and Jung Y C 2006 Micro- and nanoscale characterization of hydrophobic and hydrophilic leaf surfaces *Nanotechnology* **17** 2758–72

Bhushan B and Jung Y C 2007 Wetting study of patterned surfaces for superhydrophobicity *Ultramicroscopy* **107** 1033–41

Bhushan B, Nosonovsky M and Jung Y C 2007 Towards optimization of patterned superhydrophobic surfaces *J. R. Soc. Interface* **4** 643–8

Bico J, Marzolin C and Quere D 1999 Pearl drops *Europhys. Lett.* **47** 220–6

Bico J, Thiele U and Quere D 2002 Wetting of textured surfaces *Colloids Surf.* A **206** 41–6

Bourges-Monnier C and Shanahan M E R 1995 Influence of evaporation on contact angle *Langmuir* **11** 2820–9

Brugnara M, Della Volpe C, Siboni S and Zeni D 2006 Contact angle analysis on polymethylmethacrylate and commercial wax by using an environmental scanning electron microscope *Scanning* **28** 267–73

Burton Z and Bhushan B 2005 Hydrophobicity, adhesion and friction properties of nanopatterened polymers and scale dependence for MEMS/NEMS *Nano Lett.* **5** 1607–13

Burton Z and Bhushan B 2006 Surface characterization and adhesion and friction properties of hydrophobic leaf surfaces *Ultramicroscopy* **106** 709–16

Callies M and Quere D 2005 On water repellency *Soft Matter* **1** 55–61

Cassie A and Baxter S 1944 Wettability of Porous Surfaces *Trans. Faraday Soc.* **40** 546–51

Choi S E, Yoo P J, Baek S J, Kim T W and Lee H H 2004 An ultraviolet-curable mold for sub-100 nm lithography *J. Am. Chem. Soc.* **126** 7744–5

Coulson S R, Woodward I and Badyal J P S 2000 Super-repellent composite fluoropolymer surfaces *J. Phys. Chem.* B **104** 8836–40

Danilatos G D and Brancik J V 1986 Observation of liquid transport in the ESEM *Proc. 44th Annual Mtg EMSA* pp 678–9

Erbil H Y, Demirel A L and Avci Y 2003 Transformation of a simple plastic into a superhydrophobic surface *Science* **299** 1377–80

Erbil H Y, McHale G and Newton M I 2002 Drop evaporation on solid surfaces: constant contact angle mode *Langmuir* **18** 2636–41

Extrand C W 2002 Model for contact angle and hysteresis on rough and ultraphobic surfaces *Langmuir* **18** 7991–9

Extrand C W 2004 Criteria for ultralyophobic surfaces *Langmuir* **20** 5013–8

Feng L, Li S, Li Y, Li H, Zhang L, Zhai J, Song Y, Liu B, Jiang L and Zhu D 2002 Super-hydrophobic surfaces: from natural to artificial *Adv. Mater.* **14** 1857–60

He B, Patankar N A and Lee J 2003 Multiple equilibrium droplet shapes and design criterion for rough hydrophobic surfaces *Langmuir* **19** 4999–5003

Hozumi A and Takai O 1998 Preparation of silicon oxide films having a water-repellent layer by multiple-step microwave plasma-enhanced chemical vapor deposition *Thin Solid Films* **334** 54–9

Israelachvili J N 1992 *Intermolecular and Surface Forces* 2nd edn (London: Academic)

Jung Y C and Bhushan B 2006 Contact angle, adhesion and friction properties of micro- and nanopatterned polymers for superhydrophobicity *Nanotechnology* **17** 4970–80

Jung Y C and Bhushan B 2007 Wetting transition of water droplets on superhydrophobic patterned surfaces *Scr. Mater.* **57** 1057–60

Jung Y C and Bhushan B 2008 Wetting behavior during evaporation and condensation of water microdroplets on superhydrophobic patterned surfaces *J. Microsc.* at press

Kasai T, Bhushan B, Kulik G, Barbieri L and Hoffmann P 2005 Micro/nanotribological study of perfluorosilane SAMs for antistiction and low wear *J. Vac. Sci. Technol.* B **23** 995–1003

Kijlstra J, Reihs K and Klami A 2002 Roughness and topology of ultra-hydrophobic surfaces *Colloids Surf.* A **206** 521–9

Koch K, Dommisse A and Barthlott W 2006 Chemistry and crystal growth of plant wax tubules of lotus (*Nelumbo nucifera*) and nasturtium (*Tropaeolum majus*) leaves on technical substrates *Cryst. Growth Des.* **6** 2571–8

Koinkar V N and Bhushan B 1997 Effect of scan size and surface roughness on microscale friction measurements *J. Appl. Phys.* **81** 2472–9

Lafuma A and Quéré D 2003 Superhydrophobic states *Nat. Mater.* **2** 457–60

Lau K K S, Bico J, Teo K B K, Chhowalla M, Amaratunga G A J, Milne W L, McKinley G H and Gleason K K 2003 Superhydrophobic carbon nanotube forests *Nano Lett.* **3** 1701–5

Li W and Amirfazli A 2005 A thermodynamic approach for determining the contact angle hysteresis for superhydrophobic surfaces *J. Colloid Interface Sci.* **292** 195–201

Marmur A 2003 Wetting on hydrophobic rough surfaces: to be heterogeneous or not to be? *Langmuir* **19** 8343–8

McHale G, Aqil S, Shirtcliffe N J, Newton M I and Erbil H Y 2005 Analysis of droplet evaporation on a superhydrophobic surface *Langmuir* **21** 11053–60

Miwa M, Nakajima A, Fujishima A, Hashimoto K and Watanabe T 2000 Effects of the surface roughness on sliding angles of water droplets on superhydrophobic surfaces *Langmuir* **16** 5754–60

Neinhuis C and Barthlott W 1997 Characterization and distribution of water-repellent, self-cleaning plant surfaces *Ann. Botany* **79** 667–77

Nosonovsky M and Bhushan B 2005 Roughness optimization for biomimetic syperhydrophobic surfaces *Microsyst. Technol.* **11** 535–49

Nosonovsky M and Bhushan B 2006a Stochastic model for metastable wetting of roughness-induced superhydrophobic surfaces *Microsyst. Technol.* **12** 231–7

Nosonovsky M and Bhushan B 2006b Wetting of rough three-dimensional superhydrophobic surfaces *Microsyst. Technol.* **12** 273–81

Nosonovsky M and Bhushan B 2007a Hierarchical roughness makes superhydrophobic states stable *Microelectron. Eng.* **84** 382–6

Nosonovsky M and Bhushan B 2007b Hierarchical roughness optimization for biomimetic superhydrophobic surfaces *Ultramicroscopy* **107** 969–79
Nosonovsky M and Bhushan B 2007c Biomimetic superhydrophobic surfaces: multiscale approach *Nano Lett.* **7** 2633–7
Nosonovsky M and Bhushan B 2007d Multiscale friction mechanisms and hierarchical surfaces in nano-and bio-tribology *Mater. Sci. Eng.* R at press
Nosonovsky M and Bhushan B 2008 Patterned non-adhesive surfaces: superhydrophobicity and wetting regime transitions at press
Oner D and McCarthy T J 2000 Ultrahydrophobic surfaces. Effects of topography length scales on wettability *Langmuir* **16** 7777–7782
Patankar N A 2003 On the modeling of hydrophobic contact angles on rough surfaces *Langmuir* **19** 1249–53
Patankar N A 2004 Transition between superhydrophobic states on rough surfaces *Langmuir* **20** 7097–102
Poon C Y and Bhushan B 1995 Comparison of surface roughness measurements by stylus profiler, AFM and non-contact optical profiler *Wear* **190** 76–88
Reyssat M, Pepin A, Marty F, Chen Y and Quere D 2006 Bouncing transitions on microtextured materials *Europhys. Lett.* **74** 306–12
Rowan S M, Newton M I and McHale G 1995 Evaporation of microdroplets and the wetting of solid surfaces *J. Phys. Chem.* **99** 13268–71
Shibuichi S, Onda T, Satoh N and Tsujii K 1996 Super-water-repellent surfaces resulting from fractal structure *J. Phys. Chem.* **100** 19512–7
Stelmashenko N A, Craven J P, Donald A M, Terentjev E M and Thiel B L 2001 Topographic contrast of partially wetting water droplets in environmental scanning electron microscopy *J. Microsc.* **204** 172–83
Tambe N S and Bhushan B 2004 Scale dependence of micro/nano-friction and adhesion of MEMS/NEMS materials, coatings and lubricants *Nanotechnology* **15** 1561–70
Wagner P, Furstner F, Barthlott W and Neinhuis C 2003 Quantitative assessment to the structural basis of water repellency in natural and technical surfaces *J. Exp. Botany* **54** 1295–303
Wenzel R N 1936 Resistance of solid surfaces to wetting by water *Ind. Eng. Chem* **28** 988–94
Wier K A and McCarthy T J 2006 Condensation on ultrahydrophobic surfaces and its effect on droplet mobility: ultrahydrophobic surfaces are not always water repellent *Langmuir* **22** 2433–6
Yoon E S 2006 personal communications (KIST Seoul, Korea)
Yoshimitsu Z, Nakajima A, Watanabe T and Hashimoto K 2002 Effects of surface structure on the hydrophobicity and sliding behavior of water droplets *Langmuir* **18** 5818–22
Zhang X, Tan S, Zhao N, Guo X, Zhang X, Zhang Y and Xu J 2006 Evaporation of sessile water droplets on superhydrophobic natural lotus and biomimetic polymer surfaces *ChemPhysChem* **7** 2067–70